Wear 580-581 (2025) 206295

Contents lists available at ScienceDirect

Wear

journal homepage: www.elsevier.com/locate/wear

A novel grey-box based friction model for a wide range of machining conditions

Jan Wolf [a,*], Nithin Kumar Bandaru [b], Martin Dienwiebel [b,c], Hans-Christian Möhring [a]

[a] Institute for Machine Tools (IfW), University of Stuttgart, Holzgartenstraße 17, 70174, Stuttgart, Germany
[b] Institute for Applied Materials (IAM), Microtribology Center μTC, Karlsruhe Institute of Technology, Straße am Forum 7, 76131, Karlsruhe, Germany
[c] Fraunhofer Institute for Mechanics of Materials (IWM), Wöhlerstraße 11, 79108, Freiburg, Germany

ARTICLE INFO

Keywords:
Grey-box model
Cutting
Tribometer
Material model

ABSTRACT

Modelling the friction behaviour of cutting tools is a vital step towards understanding the complex tribo-mechanical system in cutting necessary for further improving coatings. However, measuring the friction behaviour during actual cutting is challenging due to its dependence on locally changing process conditions along the cutting tool such as sliding velocity and normal pressure. Thus this study introduces a novel tribometer to identify friction coefficients under a wide variety of normal pressures (914.7 MPa–2170 MPa) and sliding velocities (20 m/min to 250 m/min) relevant for machining. Subsequently, the adhesive friction coefficient is determined inversely by modelling the experiments via Finite Element Analysis. The wear behaviour of coated pins is discussed for a wide range of contact pressures and sliding velocities relevant for cutting. A custom Python interface is presented which enables the local prediction of velocity and normal pressure dependent friction coefficients along the cutting edge within machining simulations. Common machine learning libraries can therefore directly be introduced in the FEA engine. Supervised machine learning regression models are trained and evaluated regarding their predictive capability. The Grey-Box model allows the AI-based local prediction of friction coefficients in cutting simulations based on the process conditions at the tool-chip interface.

1. Introduction

Based on the resulting increase in simulation results accuracy, finite element analysis (FEA) has become an important tool in the domain of cutting. This development enabled the optimization of process parameters and tool geometries, leading to reduced manufacturing costs [1]. The overall accuracy of FEA modelling largely depends on the mathematical input models, which have to be determined for a distinct coupled thermo-mechanical load spectrum with extreme process conditions at high strain rates, temperatures, sliding velocities and contact pressures found in cutting. The determination of such models often does not allow the direct application of conventional laboratory equipment. A key area of interest is the modelling of frictional behaviour between tool and workpiece, which is crucial for understanding tool-chip interactions and improving wear resistance in high-speed cutting operations.

The coefficient of friction (*COF*) is difficult to measure under cutting conditions due to its dependency on contact pressure, sliding velocity, temperature, and tool wear. As these thermo-mechanical loads are varying along the cutting edge, studying the frictional behaviour during actual cutting operations by measuring cutting forces will not yield detailed insights in the dependence of the *COF* on all influencing parameters named above. Therefore, modelling friction in the secondary deformation zone remains an active area of research. As outlined by Melkote et al. [2], modelling the friction behaviour with a constant *COF* based on Coulomb's law of friction is done in current and past practice. Although it is known that this practice is a vast simplification of the real frictional behaviour, it is applied due to its comparably effortless determination with orthogonal cutting test benches as shown by Abouridouane et al. [3], which are present in many research institutes. With a given rake angle and measured cutting force and feed force, a single *COF* can be determined according to Merchant [4] in equation (1), where F_c and F_t are the cutting force and feed force respectively and γ is the orthogonal rake angle.

$$\mu = \frac{F_t + F_c \tan\gamma}{F_c + F_t \tan\gamma} \tag{1}$$

This article is part of a special issue entitled: Grey Box Wear Prediction_invited only published in Wear.

* Corresponding author.
E-mail address: jan.wolf@ifw.uni-stuttgart.de (J. Wolf).

https://doi.org/10.1016/j.wear.2025.206295
Received 30 May 2025; Received in revised form 12 August 2025; Accepted 14 August 2025
Available online 16 August 2025

This approach enables inverse determination of a fitting *COF* by aligning FEA outputs (cutting forces, chip thickness, contact length) with experimental measurements. As reported by Filice et al. [5], the same benefits apply for constant shear friction models in equation (2), which assumes a fraction m of the shear flow stress of the workpiece material k to be constant along the rake face.

$$\tau = m\,k \tag{2}$$

Despite these benefits, a friction model with a constant *COF* was found to not describe the friction process precisely which lead to further studies, where the *COF* is defined as a function. Du et al. [6] formulated a friction model solely dependent on the tool geometry as shown in equation (3), where they considered flank wear *VB*, cutting blunt radius r_n, rake angle and clearance angle.

$$\mu = tan\left[\frac{\pi}{4} + \gamma_0 + \alpha_0 \text{-} arccos\left(1 \text{-} \frac{VB}{r_n} sin\,\alpha_0\right)\right] \tag{3}$$

Here, tool wear is assumed to be a good indicator of friction development, as it leads to higher thermo-mechanical loads. However, crater wear is not considered which would be of interest for the secondary deformation zone. Zorev introduced a hybrid friction model distinguishing between sticking and sliding zones on the rake face, with Coulomb's friction law being applied in the sliding region whereas in the sticking region the frictional stress is set to the shear flow stress of the workpiece material. This then results in equation (4).

$$\tau(x) = \begin{cases} \mu\,\sigma(x) & \tau < k \\ k & \tau \geq k \end{cases} \tag{4}$$

The challenge to identify friction coefficients for the sliding zone under cutting conditions still exists in Zorev's model. Further studies thus focused on the implementation of a sliding velocity dependent Coulomb's friction model for the sliding region [7] while at the same time neglecting the influence of contact pressure, temperature and wear on the *COF*.

Zanger et al. [8] later studied the influence of normal force, sliding velocity and temperature, on the *COF* by utilizing a laboratory tribometer and formulated friction models dependent on one individual parameter and then all parameters combined. After including the models in FEA, they found the best model was the one depending on normal force and sliding velocity, however the adequateness of the range of the applied normal loads of maximum 40N to resemble cutting experiments is disputable which is why other researches build custom tribometers omitting usual limitations of standard laboratory equipment. These tribometers are fitted into a lathe or milling centre, which feature spindles with multiple hundred rounds per minute and thus, depending on the diameter of the disk, enable high-speed friction tests.

In [9], Olsson et al. build a pin on disc tribometer on a lathe, where a pin was placed behind a cutting insert to ensure a steadily refreshed surface for the pin. Despite it being able to reproduce high temperatures and velocities, it lacked high enough normal loads. Ben Abdelalo et al. [10] later build a tribometer based on a hydraulic jack, to reach normal pressures over 1 GPa. Further, they stated that their tribometers working range started at normal pressures of 1 GPa, thus studying lower normal pressures could not be achieved. Whether this was due to the hydraulic pressure generator, instability of the system or the chosen hydraulic jack was not discussed. Smolenicki et al. [11] used a loaded spring with 430 N of normal force closely behind a cutting insert. In a comparative study conducted by Schulze et al. [12], a tribometer with a spring loaded pin fitted to a 4 axis milling machine (IFT, TU Wien), a pneumatically actuated tribometer (IWF, ETH Zürich), a hydraulically actuated tribometer (ENISE Lyon) and a laboratory tribometer (IAM, KIT) were studied with one conclusion beeing that the natural frequencies ot the setups paired with the dynamics of the experiments influence the determination of *COF*. The tribometer of ENISE Lyon applied the highest normal loads and measured lower *COF* than those of the other setups. As the researchers from ENISE Lyon did not present any low-force measurements in this study, a final conclusion regarding the superiority of hydraulically actuated tribometers - were the incompressibility of fluids is exploited - over spring-loaded or pneumatically actuated tribometers is not possible. The same setup was used by Rech et al. [13] to study the heat partition coefficient during friction tests. As noted by Leveille et al. [14], the tribometers featuring a refreshed surface by placing a cutting insert in front of the pin have in common, that they cannot reach a given temperature since the temperature of the fresh surface is not set by a control system. To solve this, they fitted a laser head in an already existing tribometer to control the temperature up to 600 °C.

Another analogy setup was developed by Puls et al. [15] and was derived from orthogonal cutting. They used a cutting insert with an extremely negative rake angle on an orthogonal cutting test bench with limited cutting depth which prohibited the formation of a chip and thus formed the workpiece. By measuring the normal and tangential forces as well as the temperature, they formulated an equation to predict the *COF* depending on temperature and introduced a thermal softening term also found in the Johnson-Cook material model. Despite good agreement of simulated and experimental cutting forces and temperatures, the "depth of cut" which is expected to heavily interact with the applied normal loads or the true sliding velocity in the contact zone was not studied.

Besides the challenging part of determining suitable *COF* under cutting conditions and building custom tribometers, another issue with friction modelling is mentioned in literature and concerns the implementation of more elevated models in common FEA engines. In the literature review conducted by Melkote et al. [2], the subroutine VFRIC in ABAQUS Explicit utilized in two studies is named. Puls et al. [15] concluded with respect to the model proposed by Zorev, that their model might not be universally valid but pointed out the convenience of integrating it into an FEA engine. Arrazola et al. [16] also observed that many studies still use a mean friction coefficient due to the unavailability of complex friction models in some commercially available FEA softwares - although FEA software integrated more modelling approaches since their research was published. In recently published findings on friction modelling by Volke et al. [17], an exponential function is used to approximate the dependence of the *COF* on the sliding velocity. This regression approach, commonly done in the form of an exponential function, might be challenging for a high dimensional input, e.g. considering temperature, sliding speed, normal pressure, coating wear etc. in one model. However, artificial intelligence is known to capture high-dimensional non-linear behaviour and is able to approximate a function via a regression approach. Despite these proven benefits, the integration of AI to perform predictions during FEA is rarely adopted and ongoing research. Although solving optimization problems for the identification of model parameters such as for the Johnson-Cook material model by Hardt et al. [18], the prediction of flow stress dependent on temperature, strain and strain rate was just recently predicted with an artificial neural network within a VUHARD subroutine in ABAQUS Explicit by Ducobu et al. [19]. According to the authors, this was the first AI based material model for modelling of cutting operations. However, they required to add a substep where the trained Python model needed to be converted to a Fortran model to integrate it in the subroutine.

To the best of the authors knowledge no AI based prediction of friction coefficients during FEA modelling of cutting has been proposed despite the benefits of considering multiple input parameters. This study therefore proposes a novel Grey-Box framework for efficient friction prediction of coated cutting tools by focusing on the following subtasks – each of which is addressed in a separate chapter of this paper: A tribometer for the identification of *COF* under cutting conditions – meaning varying sliding velocities and normal pressures - is designed and its behaviour is analysed. The tribometer is then used to generate a large dataset of *COF* under machining conditions. The impact of varying load spectrums on the wear of coated pins is analysed for conducted wear experiments. A subsequent inverse optimization study is performed to

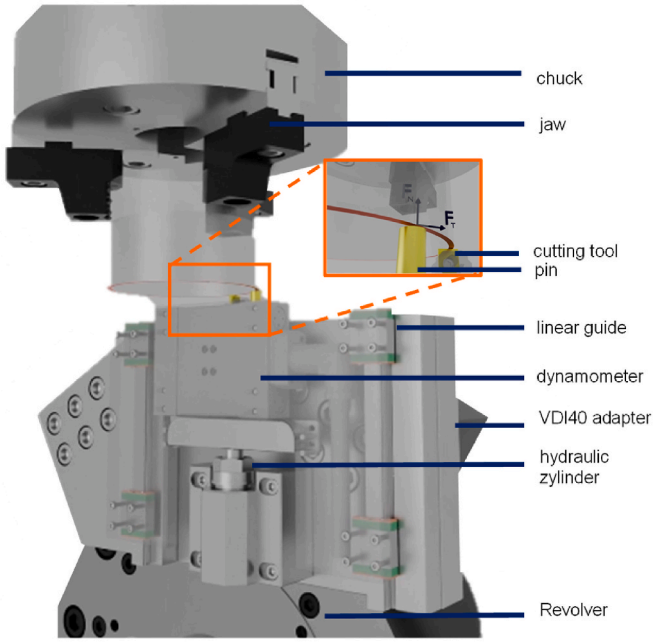

Fig. 1. Design of the optional open or closed tribometer fitted on EMAG VLC 250 vertical lathe center.

determine the adhesive *COF* for improved friction modelling. Multiple AI models are trained and evaluated regarding their predictive capabilities depending on the two input parameters of normal pressure and sliding velocity. Finally, a custom implementation of a Python interface for the seamless integration of common AI libraries into the commercial FEA software DEFORM without the need of previously mentioned conversion of algorithms into different source code is presented.

2. Design of the tribometer

In order to study the frictional behaviour of a TiN/AlTiN coated cutting tool, a tribometer based on the pin-on-disk concept is designed and fitted to a lathe which is depicted in Fig. 1. The setup features standard measurement equipment available at most modern machining labs. It utilizes a multicomponent dynamometer type 9119AA2 by Kistler rated for up to 4 kN to capture the normal and tangential forces applied on the tip of the pin. The normal force is applied by a HAWE 16-8 hydraulic cylinder. It is rated for up to 10 kN at a hydraulic pressure of 500 bar. A Röhmheld hydraulic power unit type 7.1600 is installed, providing a maximum pressure of 500 bar and a flow rate of 0.82 l/min. MGN12 linear rail guides from HIWIN are used to guide the dynamometer in z-direction if hydraulic pressure is applied. Pins with radius 8 mm made of the same material as cutting inserts were grinded to form a pin and subsequently PVD coated by Paul Horn GmbH to resemble their EG5 coating. The base plate is connected to two custom made VDI40 tool holders. All machined steel parts are made of Toolox33. Between the VDI tool holders on the revolver exists a slot to mount a cutting tool with a standard VDI 40 vertical adapter. Thus, the presented tribometer can be used as an open tribometer, where a cutting insert, which is placed in front of the pin, machines a workpiece while the pin glides over a freshly generated surface under cutting temperature and with cutting velocity. This requires the spindle to be moved with a set feed rate in z-direction. To guarantee a collision-free experiment, the hydraulic pressure is controlled via a manual switch. The second configuration allows to study the friction behaviour with a closed tribometer, where no tool is refreshing the surface in front of the pin and thus the pin enters the old wear track after one revolution of the spindle. The second setup is used in this study.

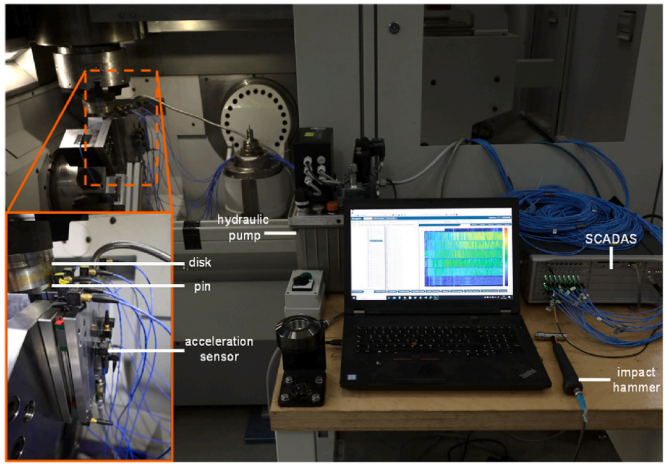

Fig. 2. Experimental setup for modal analysis.

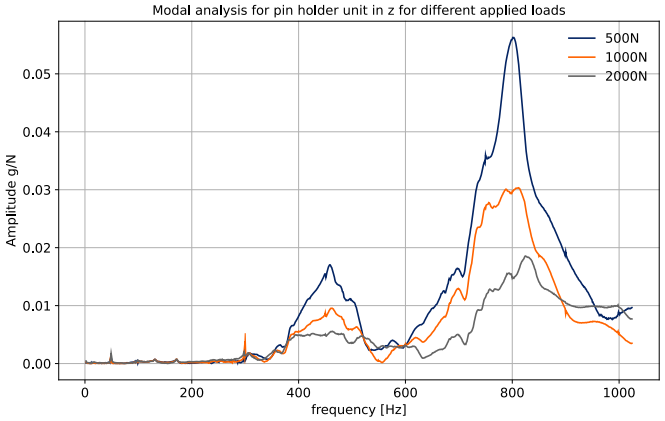

Fig. 3. Results of the modal analysis for the acceleration sensor next to the pin.

2.1. System characterization of the developed tribometer

During the construction of the tribometer test-stand it was noted that existing tribometers were not fully characterized in previous works, making it difficult to gain insights in their behaviour and further limiting comparability. As the tribometers are run under machining like conditions with high loads and utilizing a spindle with up to multiple hundred rotations per minute in the experiments, the dynamic behaviour of the setup needs to be studied for a transparent judgement of the contact behaviour between the pin and the disk and thus allowing the future comparison of setups.

A modal analysis was conducted to judge the behaviour of the system. The works of Schulze et al. [12] served as a motivator for that, as they conducted a comparison of different tribometers and found significant differences in the determined *COF*. The experimental setup is depicted in Fig. 2. Multiple triaxial acceleration sensors were mounted to the setup. Then the hydraulic pump was activated and the pin moved upwards towards the positioned workpiece. Then an impact hammer was utilized to excite the structure. This was repeated with three different normal loads of 500 N, 1000 N and 2000 N to study the influence of the normal force on the structure. The forces were chosen in accordance to typical average hertzian contact pressures at the rake face, the cutting edge and flank face which is further explained in section 5. Findings are shown in Fig. 3. It can be noted, that a higher normal load led to a better vibrational behaviour as the amplitude dropped noticeably. From this perspective, a higher normal load combined with a larger r value of the pin's tip, which leads to a similar result of the normal

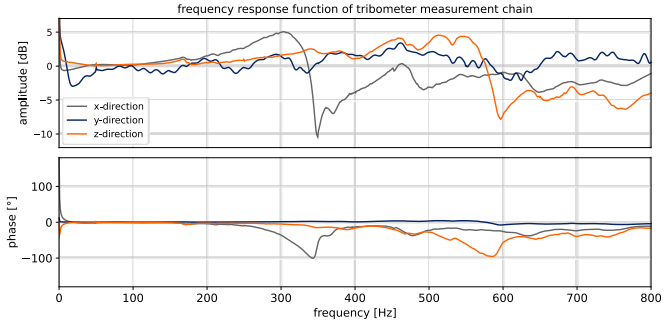

Fig. 4. Frequency response function (FRF) of tribometer force-measurement chain.

Fig. 5. Pin after grinding (left) and after PVD coating (right).

pressure, might be targeted by researchers in further studies.

The experiments were conducted on an EMAG VLC 250 vertical lathe machine. A multi-channel charge amplifier Kistler type 5070 was used. The dynamic behaviour of the dynamometer and the charge amplifier needs to be determined to allow for a reasonable measurement of the forces and the resulting evaluation of the measurements. Thus, an impact testing was performed in advance of the experiments to determine the frequency response function (FRF) of the measurement chain. Simcenter SCADAS by Siemens is used for this task where an impact hammer is chosen as the reference and the output of the charge amplifier is the input signal for determination of the FRF. The results of the analysis are shown in Fig. 4. The dynamic analysis of the tribometer revealed that the resonant frequencies are at least an order of magnitude higher than the excitation frequency of the spindle. Therefore, the dynamic behaviour of the tribometer was not considered further in the evaluations.

3. Identification of friction coefficients

Frictional behaviour is studied by utilizing pins which are grinded to a tip radius of 17 mm and then PVD coated by Paul Horn GmbH according to their EG5 coating made up of an aluminium titanium nitride (AlTiN) and a titanium nitride (TiN) coating which is also used on regular cutting tools. The pins are depicted in Fig. 5.

A full factorial experimental plan with the variables sliding velocity and normal pressure was implemented. In total 10 normal loads were chosen ranging from 150 N to 2000 N and equidistantly spaced. A new

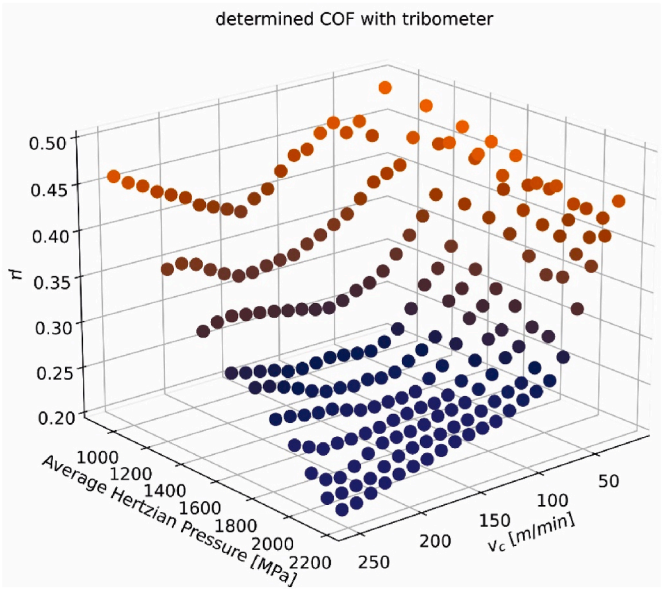

Fig. 6. Influence of sliding velocity and normal load on determined *COF*.

pin is used for each normal load. The normal load is regulated by adjusting the target pressure of the hydraulic power unit until the target normal force is reached. Then 21 different sliding velocities are programmed and equidistantly spaced ranging from 20 m/min to 250 m/min. Due to the selected velocity range, the maximum sliding speed closely resembles typical cutting velocities. The chosen combination of normal loads and sliding velocities therefore effectively represents the mechanics of conventional cutting processes, as later demonstrated in Fig. 15.

Upon reaching the corresponding spindle rpm, the velocity stalls for 0.5 s before being increased to the next step. Forces are recorded via a Labview script with a frequency of 1000 Hz. Recording of forces is triggered from the G-Code, by applying voltage to an output pin of the Numerical Control Unit (NCU). Thus, the measured *COF* were averaged in intervals of 0.5 s.

This study utilizes normalized AISI 1045. AISI 1045 is one of the most commonly used medium carbon steels in industry. Studying the frictional behaviour of this steel in combination with commonly applied tool coatings therefore provides practical value for a wide range of real-world applications. With respect to DIN EN ISO 683-1 the data in Table 1 has been collected. Furthermore, the grain size is greater or equal to 5 µm with respect to DIN EN ISO 643 and the Brinell hardness ranges from 178 to 180 HBW with respect to DIN EN ISO 6506.

The resulting dataset made up of 210 samples is plotted in Fig. 6, where a strong dependency of the *COF* on sliding velocity and contact pressure is obvious. These findings contradict the conclusion of Zemzemi et al. [20], who observed no dependency of the *COF* on normal pressure when applying 500 N and 1000 N to a TiN-coated pin with AISI4142 as the workpiece material. In a brief discussion they highlighted that the findings are contradicting with common research and suggested, that the material combination might be the reason. However, the preliminary experiments conducted by Smolenicki et al. [11] with their spring-loaded tribometer also concluded that contact pressure has a negligible influence on the *COF* despite using the same material combination - a TiAlN + TiN-coated pin and AISI1045 - as in this study.

Table 1
Chemical composition of normalized AISI 1045 in accordance with DIN EN ISO 683-1.

C	Si	Mn	P	S	Cr	Mo	Ni	Al	Cu
0.431	0.233	0.653	0.011	0.024	0.124	0.005	0.018	0.029	0.029

No further information is given regarding the range of tested normal loads which is why one does not simply compare their results with our findings. When comparing the determined *COF* with the friction coefficients reported in a study by Schulze et al. [12], which analysed four existing tribometers, the values from the ENISE Lyon tribometer at just below 2000 MPa can be estimated from the presented plot to lie roughly between 0.26 and 0.30 for velocities of 60 m/min to 80 m/min. In our case, we obtained values between 0.29 and 0.31 for the velocity range. For comparison, the *COF* determined by TU Wien at roughly 1500 MPa can be estimated at 0.37 to 0.48 for the range of 60 m/min to 160 m/min while we determined 0.34 to 0.41 for that velocity range. Although a direct comparison of all our values with existing setups is not entirely possible, these initial comparisons indicate that our results are realistic.

4. Wear behaviour of pins

Extensive tribological investigations have consistently demonstrated the effectiveness of TiN and AlTiN coatings in enhancing the dry sliding wear performance of steel substrates, these hard ceramic coatings, typically applied by physical or chemical vapour deposition (PVD/CVD), act as thermal and chemical barriers, reducing wear rates and stabilizing the *COF*. However, their tribological response is highly sensitive to mechanical parameters such as normal load and sliding speed, as well as environmental factors like the presence or absence of oxygen.

Singer et al. [21] reported that surface roughness significantly affects the friction behaviour of TiN in air. Tests using steel balls on TiN-coated substrates showed high initial *COF* values (0.5–0.7) for rough coatings (R_a = 60–100 nm), while polished TiN surfaces ($R_a \approx 4$ nm) reduced initial *COF* to 0.15–0.2. Despite these improvements, prolonged sliding caused the *COF* to increase due to the accumulation of oxide debris. Auger spectroscopy and transmission electron microscopy revealed the formation of metallic iron, iron oxide, and titanium oxide on the steel counterfaces, supporting an oxide-mediated wear mechanism. This finding aligned with the interpretation by Wilson and Alpas [22,23] who described the process as “oxide wear”, emphasizing the key role of tribo-oxide formation in reducing friction and stabilizing wear performance under ambient conditions.

Wilson and Alpas [22,23] further developed wear mechanism maps for TiN coatings under dry conditions using pin-on-disk tests with AISI M2 high-speed steel. Their studies revealed four distinct wear regimes based on the interplay between load, speed, and interface temperature. At low loads (<10 N) and low speeds (<0.5 m/s) rapid oxidation and tribochemical polishing dominated. Increasing load or speed moved the system into a mild wear regime (Regime II), characterized by the abrasive removal of TiN asperities and iron-rich debris compaction into surface valleys. At loads exceeding ~100 N and moderate speeds, Regime III initiated, wherein TiN softened thermally (150–200 °C), leading to preferential wear and exposure of the substrate. Interestingly, further increasing the sliding speed resulted in a return to mild wear (Regime IV) due to the softening of the opposing steel pin at temperatures exceeding 300 °C, which diminished its abrasiveness. Across these regimes, wear mechanisms such as delamination, flaking, ploughing, and spallation were frequently observed, along with the development of tribo-oxide layers.

Kara et al. [24] extended this understanding to vacuum environments. Their study on TiN-coated AISI 52100 steel highlighted how oxidation availability controls tribo-performance. Under ambient conditions, oxides such as TiO_2 and $FeTiO_3$ formed protective layers, resulting in lower wear rates (e.g., 2.78×10^{-14} $m^3/(N{\cdot}m)$). In contrast, vacuum conditions inhibited oxide formation, leading to increased adhesive wear, plastic deformation, and higher wear rates. The chemical nature of the oxide (TiO_2 vs. $FeTiO_3$) was found to correlate with wear protection efficacy. Regarding AlTiN coatings, several studies have demonstrated their improved performance under high thermal loads due to enhanced oxidation resistance. Zheng et al. [25] investigated TiAlN/TiN multilayer coatings and observed that *COF* decreased with increasing sliding speed but increased with load, ranging from 0.40 to 0.65. The wear rate decreased with sliding speed and load, driven by oxide layer formation and tribofilm stabilization. Dominant wear mechanisms included adhesion, delamination, oxidation, and micro-chipping. Notably, multilayer architectures outperformed single-layer TiN or TiAlN coatings in resisting crack propagation and tribo-fatigue failure. In a study using AlTiN-coated WC-Co against Ti6Al4V Tebaldo et al. [26] reported that AlTiN increased friction due to reduced adhesive transfer from the counterface. This suggests AlTiN may hinder beneficial tribolayer formation, depending on the tribopair. Nonetheless, its resistance to plastic deformation and abrasive wear made it more suitable under aggressive cutting or sliding conditions. These results highlight the material-specific nature of tribological interactions and the importance of testing within the intended application context. Król et al. [27] offered insights into the C45 steel counterface by evaluating oxidized titanium pins sliding against hardened C45 steel. Although TiN or AlTiN were not used, their findings showed that surface oxidation of titanium led to a ~160-fold reduction in wear rate compared to untreated titanium, with oxide-rich wear debris playing a protective role. This underscores the importance of oxide formation and debris morphology in controlling friction and wear on C45 steel interfaces.

Across all studies, several factors consistently emerge as critical in controlling the wear behaviour of TiN and AlTiN coatings: (1) tribo-oxide formation plays a central role in stabilizing friction and reducing wear in ambient conditions; (2) sliding speed and normal load determine thermal softening, wear regime transitions, and debris formation; (3) surface roughness affects initial *COF* and transfer layer formation; (4) coating hardness and thickness influence resistance to plastic deformation and spallation, though excessive thickness may lead to stress-induced failures; and (5) coating architecture and composition (e.g., multilayer TiN/TiAlN vs. single-layer coatings) modulate crack resistance and tribofilm stability. The dry sliding wear of TiN and AlTiN coatings on or against C45 steel entails a complex interplay of mechanical and tribochemical mechanisms. Friction and wear are largely governed by the development of oxide-based tribofilms, temperature-dependent softening, and the synergistic interaction between coating and counterface. TiN offers low-friction performance under moderate loads but is vulnerable to thermal degradation. AlTiN provides superior high-temperature stability and wear resistance, especially in multilayer configurations. Optimizing coating selection for specific contact conditions, including substrate type, load, speed, and environment, remains essential for maximizing performance.

To conduct further studies regarding the coating’s wear behaviour, five additional experiments were performed. As shown in Table 2, a fully factorial and equidistant experimental plan with the normal loads ranging from 150N to 2000N and sliding velocities of 20 m/min to 250 m/min were conducted.

Table 2
Experimental plan for wear-experiments.

	Load	Sliding velocity	Overall time
Pin 1	1075 N	125 m/min	45 s
Pin 2	150 N	250 m/min	30 s
Pin 3	150 N	20 m/min	2460 s
Pin 4	2000 N	20 m/min	397 s
Pin 5	2000 N	250 m/min	7 s

4.1. Wear behaviour of pins under microscopic analysis

The microscopic wear behaviour of TiN/AlTiN-coated tungsten carbide (WC) pins was systematically examined using a Keyence VHX-6000 digital microscope at magnifications of 20 × and 1000 × to capture wear features. The pins were tested under dry sliding conditions against normalized C45 steel disks, normal loads (150–2000 N), sliding

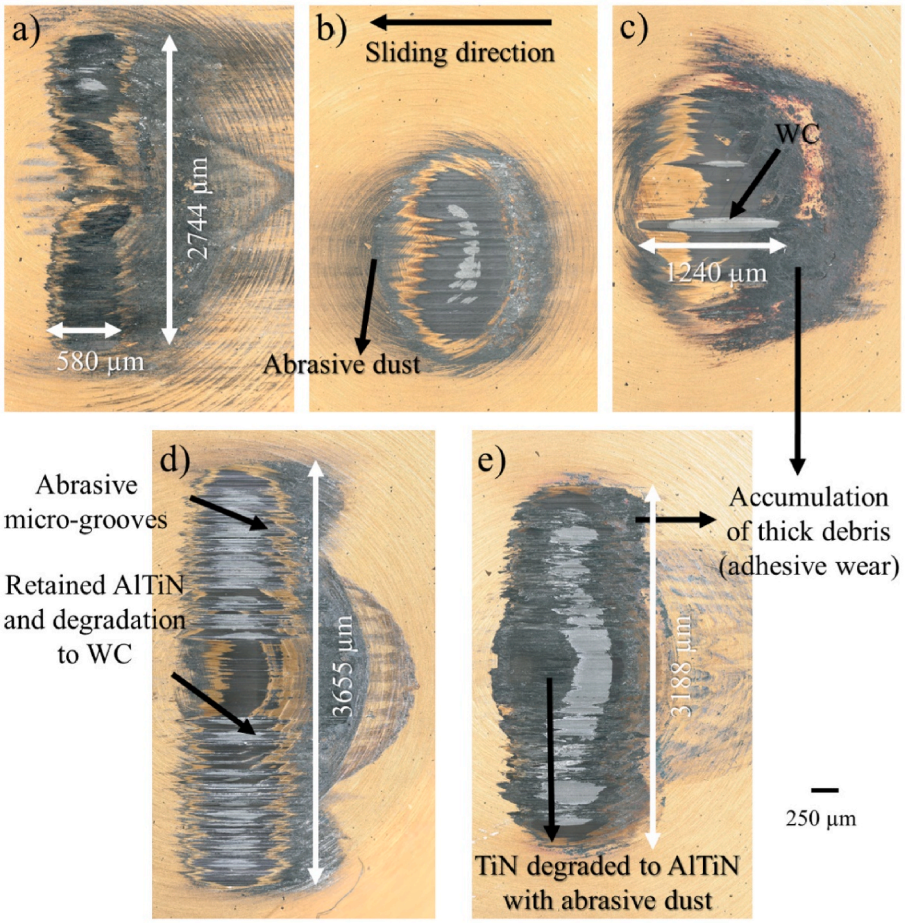

Fig. 7. (a–e). Microscopic images of pins (Pins 1–5) after dry sliding against C45 steel under varying loads, speeds, and durations.

velocities (20–250 m/min), and durations (7–2460 s), as detailed in Table 2.

Distinct wear morphology and scar dimensions were observed, strongly influenced by the tribological parameters. Pin 5, tested at an extreme combination of 2000 N and 250 m/min for 7 s, exhibited the most catastrophic coating failure (Fig. 7e). The wear scar measured approximately 3188 µm in length with a core width of ~250–500 µm and an overall affected width reaching ~1229 µm. Severe delamination of both TiN and AlTiN coatings led to full exposure of the WC substrate. Morphological features such as radial thermal cracks, central ploughing and transfer layer deposition indicate failure mechanisms dominated by short duration thermal spikes, high shear strain rates and localized coating softening, causing the coatings to fracture and shear away. In contrast, Pin 2, subjected to the same sliding speed (250 m/min) but under a lower load of 150 N for 30 s, showed a different wear (Fig. 7b). The wear scar was shorter (~1542 µm) and narrow (~280–490 µm) with only mild abrasive wear on the TiN surface and no penetration to the AlTiN or WC substrate. This contrast underlines the critical role of applied load in determining coating failure under high-speed regimes: while both samples experienced similar thermal conditions, only the Pin 5 reached the critical stress threshold for brittle delamination and substrate exposure due to higher normal load.

In comparison of Pin 2 and Pin 3 both tested under 150 N reveals the influence of sliding velocity and duration. Pin 3, run at 20 m/min for 2460 s, exhibited a longitudinal scar of ~2694 µm, with width ranging from ~480 to 1240 µm (Fig. 7c). The wear morphology showed uniform removal of the TiN top layer, while the AlTiN sublayer remained largely intact. Evidence of oxide film formation, debris accumulation, and parallel micro-scratches suggests a progression controlled by mild abrasive, oxidative, and third-body wear mechanisms over the prolonged duration. The wider wear width compared to Pin 2 implies more extensive coating fatigue and lateral material flow, despite the lower sliding speed. Further insight is gained by comparing Pin 3 and Pin 4, both tested at 20 m/min, but under drastically different loads. While Pin 3 maintained coating integrity due to its low stress, Pin 4 (2000 N, 20 m/min, 397 s) serves as a transitional case (Fig. 7d). The scar length was ~2240 µm with a central width of ~670–910 µm, featuring patchy delamination of TiN, localized AlTiN exposure and limited WC visibility. Morphological contrast and debris distribution point to a combination of adhesive, abrasive, and subsurface fatigue wear, where interfacial cracking and gradual shear-induced detachment undermined coating integrity without inducing full-scale failure.

Pin 1, tested at an intermediate load and speed (1075 N, 125 m/min, 45 s), exhibited moderate wear with a scar of ~1860 µm length and width ~430–800 µm (Fig. 7a). The TiN layer showed signs of localized thinning, while AlTiN remained mostly unaffected. Fine scratches and slight oxidation suggest early-stage micro-abrasion and thermal softening at contact asperities, but the coating stack preserved structural integrity overall. Thus, the wear behaviour across samples reflects a complex interplay between mechanical load, thermal input and sliding duration. High load and speed combinations (Pin 5) accelerated failure through delamination, cracking, and substrate exposure, while low-speed, long-duration conditions (Pin 3) resulted in gradual wear via oxidative and abrasive mechanisms without catastrophic damage. Moderate conditions (e.g., Pins 1 and 2) largely preserved coating functionality, with only surface-level TiN damage and no structural compromise. The optical findings from Keyence microscopy are further supported by high-resolution White Light Interferometry (WLI) for wear

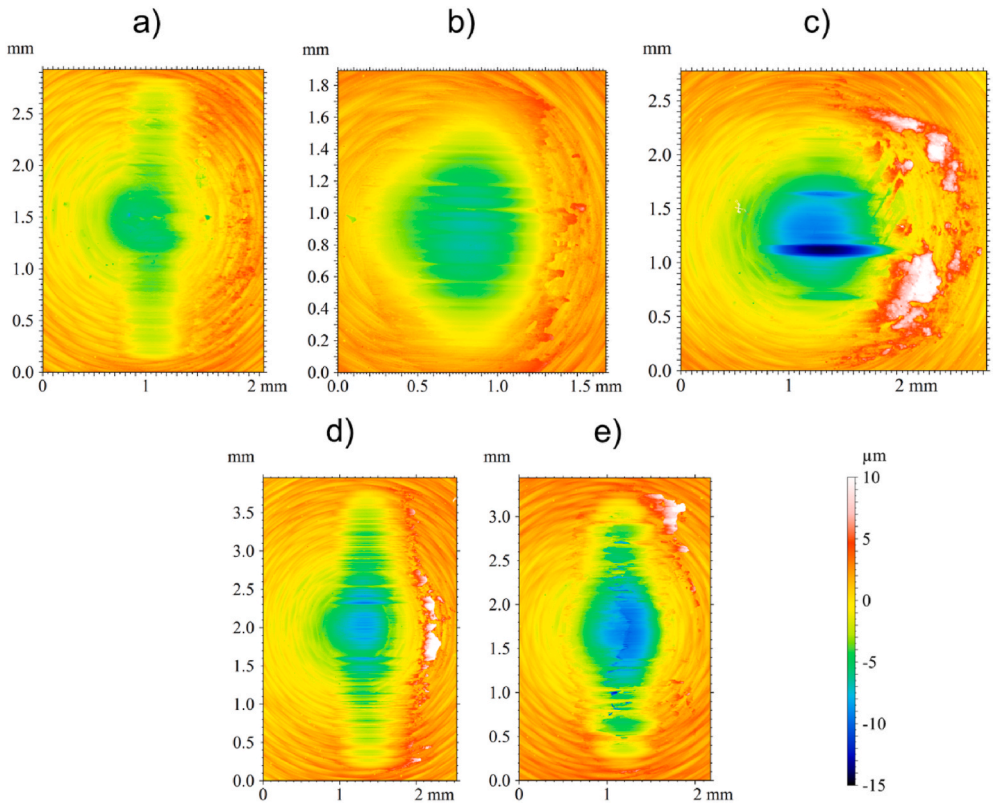

Fig. 8. (a–e). 3D WLI surface topography maps of pins (Pins 1–5) after dry sliding against C45 steel, showing variations in wear depth, debris accumulation and coating degradation under different tribological conditions.

depth profiling, Scanning Electron Microscopy (SEM) for delamination visualization, and Energy Dispersive X-ray Spectroscopy (EDX) for elemental composition.

4.2. Wear behaviour of pins under White Light Interferometry (WLI) analysis

WLI was employed to quantitatively surface degradation and wear depth. The 3D topography of the wear scars was acquired using a Polytec optical profilometer equipped with a 10 × objective lens and processed via Sensofar MountainsMap® software. This analysis enabled precise determination of mean wear depth and surface texture, thereby facilitating correlation with the coating failure mechanisms observed under optical microscopy. The WLI scan of Pin 1, tested under 1075 N and 125 m/min for 45 s, revealed a mean wear depth of 3.83 μm with a relatively uniform surface profile and smooth transition across the scar boundaries. The wear corresponds to controlled abrasive wear, where TiN was partially removed but the AlTiN sublayer remained largely preserved, optical observations in Fig. 7a.

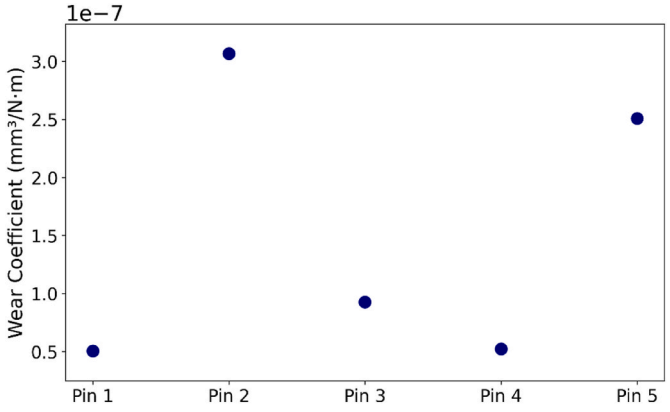

Fig. 9. Calculated wear coefficients ***K*** for varying test conditions.

In contrast, Pin 2 (150 N, 250 m/min, 30 s) showed a greater mean wear depth of 4.99 μm, despite its lower normal load. The WLI profile displayed micro-delaminated features and uneven valleys, consistent with intensified abrasive wear coupled with thermal softening due to high-speed sliding (Fig. 8b). These findings align with the surface disruption and coating thinning seen in Fig. 7b. Pin 3, which underwent long-duration testing (2460 s) at 20 m/min under 150 N, exhibited the deepest wear scar with a mean depth of 6.64 μm (Fig. 8c). The topography map revealed significant material removal with broad, deep valleys, indicative of fatigue-induced delamination, oxidative debris formation, and subsurface damage accumulating over time. This is corroborated by the micrograph in Fig. 7c, which shows extensive TiN loss and progressive exposure of the AlTiN layer.

Pin 4 (2000 N, 20 m/min, 397 s) presented a mean wear depth of 4.27 μm (Fig. 8d) with an asymmetric surface morphology featuring abrupt depth changes and lateral ridges. These features indicate mixed wear involving both adhesive and abrasive removal, driven by high contact pressures and uneven stress distribution. The corresponding microscopy image (Fig. 7d) shows partial TiN delamination and debris entrapment, confirming these WLI-based inferences. Despite its short test duration, Pin 5 (2000 N, 250 m/min, 7 s) exhibited a mean wear depth of 5.10 μm (Fig. 8e), underscoring the severe nature of thermal-mechanical overload. The WLI profile featured deep ploughing grooves, elevated rim buildup, and surface fragmentation, reflecting catastrophic coating failure observed earlier in Fig. 7e. The severity of damage after only 7 s confirms the critical interplay between peak contact stress, sliding velocity, and coating ductility limits.

In summary, detailed comparison confirms that normal load is the most critical parameter dictating coating integrity, but sliding speed and duration critically shape the failure mode. High load with high speed

(Pin 5) led to brittle, catastrophic failure, while high load with low speed (Pin 4) promoted gradual delamination through mixed wear with retained AlTiN. Low load with long duration (Pin 3) resulted in deep wear via fatigue and oxidation, whereas low load with high speed (Pin 2) caused thermal abrasion. Moderate conditions (Pin 1) achieved the lowest wear severity.

To further quantify the material property and the efficiency of the TiN/AlTiN-coated WC pins under different tribological conditions, wear coefficients were calculated based on Archard's equation (5), using wear volumes derived from WLI measurements. The wear coefficient K, expressed in $mm^3/(N{\cdot}m)$, reflects the normalized wear volume V per load F and sliding distance s, providing a robust parameter to compare wear performance across varying test conditions (Fig. 9).

$$K = \frac{V}{F\,s} \tag{5}$$

Pin 1, operated under a moderately high load (1075 N) and medium sliding speed (125 m/min) for 45 s, yielded the lowest wear coefficient of 0.50×10^{-7} $mm^3/(N{\cdot}m)$ (Fig. 9). This low value highlights the coating's ability to resist wear under balanced thermal and mechanical input. The wear depth of 3.83 μm and minimal morphological damage suggest mild abrasive wear, with effective load distribution and limited coating penetration. In contrast, Pin 2, tested at high speed (250 m/min) and low load (150 N) for 30 s, exhibited the highest wear coefficient at 3.07×10^{-7} $mm^3/(N{\cdot}m)$, as evident in (Fig. 9). Despite lower mechanical pressure, the elevated velocity significantly increased frictional heating and surface stress, suggesting accelerating TiN layer delamination and substrate exposure. The wear depth of 4.99 μm supports this interpretation of rapid material removal, indicating that thermal effects induced by high velocity can substantially influence wear behaviour, even under reduced normal loads.

Pin 3, also at 150 N but operated at a low sliding speed (20 m/min) for a duration of 2460 s, resulted in a moderate wear coefficient of 0.93×10^{-7} $mm^3/(N{\cdot}m)$ (Fig. 9), despite registering the deepest wear scar of 6.64 μm. This indicates that while total material removal was high, the normalized wear rate was dominated by the long sliding distance. The wear mechanism here was largely fatigue-driven, with oxidative debris formation and progressive coating thinning accumulating over time, rather than rapid delamination. Pin 4, which experienced the highest normal load (2000 N) at a low sliding speed (20 m/min) for 397 s, recorded a comparatively low wear coefficient of 0.52×10^{-7} $mm^3/(N{\cdot}m)$ similar to Pin 1 (Fig. 9). The wear depth was 4.27 μm, and the surface profile showed patchy delamination, adhesive wear features, and localized compaction of debris, which may have created a temporary third-body protective layer. This result suggests that under certain conditions high contact pressures can suppress material loss by stabilizing the wear interface.

Pin 5, subjected to simultaneously high load (2000 N) and high speed (250 m/min) for just 7 s, produced a wear coefficient of 2.51×10^{-7} $mm^3/(N{\cdot}m)$ (Fig. 9). While slightly lower than that of Pin 2, this reflects severe and rapid coating failure characterized by brittle fracture, ploughing and thermal cracking as evident from its 5.10 μm mean wear depth and intense damage. These results emphasize that wear behaviour cannot be predicted by load alone. While high loads do increase stress, it is the combination of sliding speed, duration and thermo-mechanical interactions that governs the wear coefficient. For instance, Pins 2 and 5 indicate that high-speed conditions, regardless of applied load, lead to rapid coating failure. Conversely, Pins 1 and 4 show that moderate or low-speed conditions, even at elevated loads, can reduce normalized wear when interfacial conditions remain stable. The integration of wear coefficients with WLI-based depth measurements and microscopy-based failure modes provides a comprehensive understanding of the tribological response of TiN/AlTiN-coated WC tools.

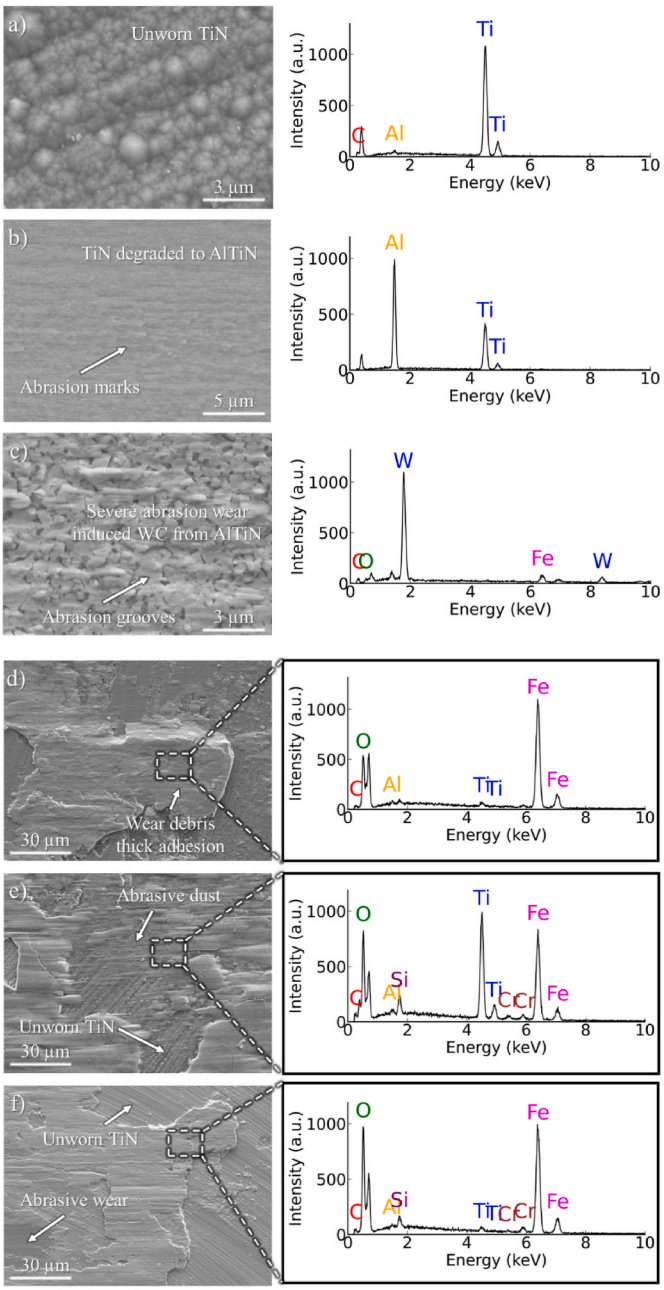

Fig. 10. (a–f). SEM images (left) and corresponding EDX spectra (right) of TiN/AlTiN-coated WC pins illustrating different wear stages and material transformations: (a) unworn coating; (b) worn until AlTiN layer; (c) worn through to WC substrate, and (d–f) transfer material.

4.3. Wear behaviour of pins under scanning electronic microscope (SEM) and energy dispersive X-ray spectroscopy (EDX) analysis

To study the wear mechanisms underlying the optical and topographical observations in Sections 4.1 and 4.2, SEM and EDX analyses were conducted on worn and unworn regions of TiN/AlTiN-coated WC pins. These analyses focused on four characteristic wear states: (i) unworn TiN surface, (ii) AlTiN-exposed regions, (iii) fully worn WC substrate areas, and (iv) debris-covered zones. Figs. 10 and 11 present high-magnification SEM micrographs with corresponding EDX spectra, offering insights into the elemental composition, microstructural degradation, and dominant wear mechanisms across different tribological regimes.

Fig. 10a depicts the unworn surface of the TiN coated WC pin. The

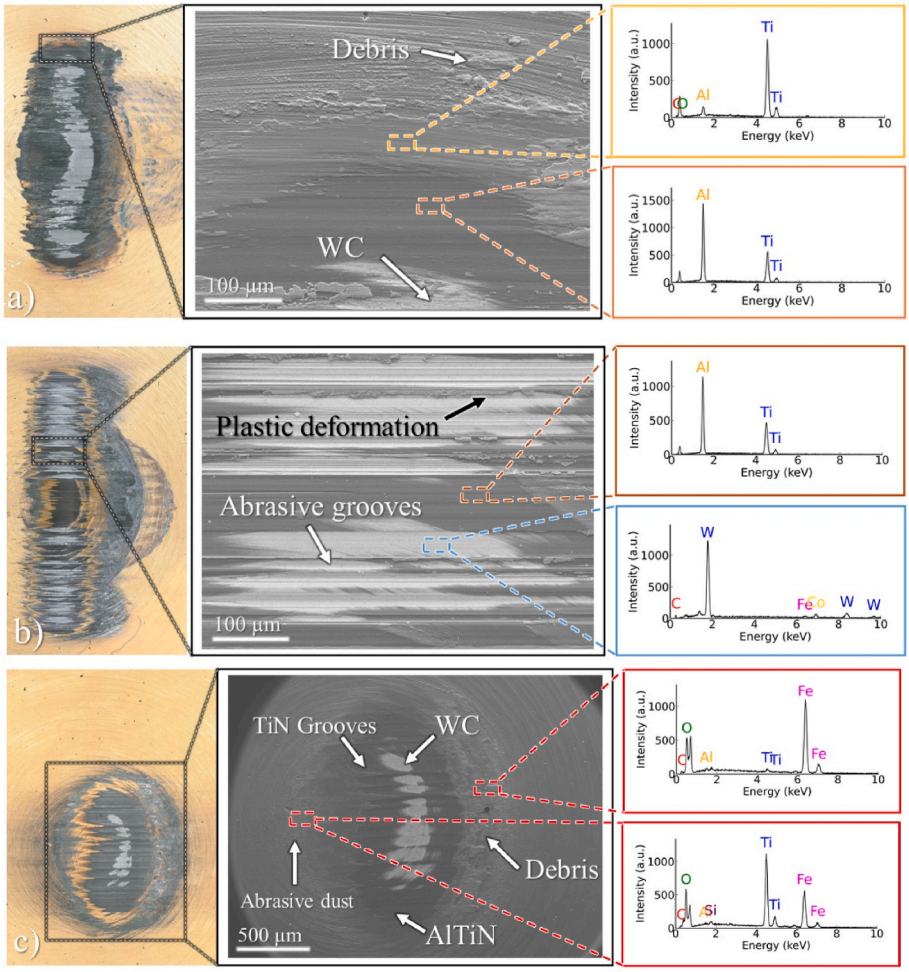

Fig. 11. Digital microscopic images (left) SEM images (center) and corresponding EDX spectra (right) of TiN/AlTiN-coated WC pins illustrating different wear: (a) Pin 5; (b) Pin 4; (c) Pin 2.

SEM image shows a dense, featureless surface indicative of a continuous TiN outer layer without surface cracking or porosity. The associated EDX spectrum confirms a high concentration and presence of a chemically stable, hard nitride surface Ti, with minor Al from the underlying AlTiN layer. In Fig. 10b, representing a region worn to the AlTiN layer, SEM imaging reveals localized delamination and surface grooves, suggesting plastic deformation under repetitive contact stress. The EDX spectrum shows clear peaks for both Ti and Al, confirming exposure of the interlayer. This transition zone indicates a stage where the TiN has failed due to cohesive fracture or interfacial shear, but the tougher AlTiN layer continues to act as a barrier. The morphology reflects moderate wear dominated by tensile stress-driven cracking and partial spallation.

Fig. 10c shows severe surface disruption where the coating has been fully breached, revealing the WC substrate. The SEM image exhibits brittle fracture features, grainsfig10, and micro-pits, indicative of substrate-level delamination. The EDX profile shows dominant peaks of tungsten (W) and cobalt (Co), and diminished Ti and Al content, confirming complete coating loss. This failure is associated with high cyclic stresses, thermal fatigue, and coating–substrate adhesion failure, often induced by long-duration or high-load sliding. This wear regime is classified as coating-through wear, where both coating layers and the bonding interface have failed. Fig. 10d–f illustrate third-body debris-covered regions. SEM imaging shows compacted wear particles, smearing, and re-solidified tribofilms, implying active third-body wear mechanisms. The EDX spectra reveal the presence of Fe, O, and Cr, with occasional Si, indicating material transfer from the C45 steel counterbody and oxidation of both contacting surfaces. These regions confirm the occurrence of adhesive wear, tribo-oxidation, and chemical interaction at elevated temperatures. The presence of oxygen-enriched debris and tribofilms implies reactive sliding, particularly under high-energy conditions (Pin 5) where localized flash temperatures can reach thresholds for surface oxidation and softening.

Fig. 11a (Pin 5 tested at 2000 N and 250 m/min for 7 s) the SEM image reveals severe coating delamination, deep ploughing grooves, and fragmented debris, indicative of rapid and catastrophic failure of both the TiN and AlTiN layers. EDX analysis performed at two distinct regions the central worn zone and the debris-affected periphery provides further insight into the failure mechanisms. In the top contact zone, the EDX spectrum shows dominant peaks of Ti and Al. Together, the SEM-EDX findings confirm a hybrid wear mechanism for Pin 5, characterized by central delamination and substrate exposure due to thermo-mechanical overload, surrounded by oxidative third-body interactions. These results align closely with the WLI-determined wear depth (5.10 µm) and the high wear coefficient (2.51×10^{-7} $mm^3/(N{\cdot}m)$), reinforcing the conclusion that under extreme sliding conditions, the coating fails rapidly through a combination of brittle fracture, adhesion, and tribochemical attack.

Fig. 11b (Pin 4 tested at 2000 N and 20 m/min for 397 s) shows a more moderate but progressive wear response despite being subjected to the same load as Pin 5. The SEM image reveals partial TiN layer delamination, AlTiN layer disruption and surface grooves with evidence of microcracks and localized wear track deformation. This morphology is consistent with a mixed adhesive abrasive wear regime, where mechanical contact stress initiated coating breakdown, but the lower

sliding velocity limits the rate and depth of material removal. EDX reveals clear signals of Ti and Al, indicating that the coating has thinned, but not fully failed, this suggests incipient AlTiN coating exposure. In the secondary region the EDX spectrum shows W element suggesting substrate exposure. This supports a mechanism involving mechanical delamination initiated by interfacial shear, followed by tribo oxidative contribution to wear in localized areas.

Fig. 11c (Pin 2 tested at 150 N and 250 m/min for 30 s) illustrates early-stage coating degradation driven by high sliding speed under a relatively low mechanical load. The SEM image shows fine abrasive scratches, incipient TiN grooves, and minimal material loss, showing the surface fatigue and thermal softening. The wear track remains relatively shallow and continuous, lacking the severe structural disruptions observed in Pins 4 and 5. The EDX analysis, conducted at two distinct surface regions, helps to further elucidate the wear mechanism. The first spectrum, acquired from a zone with thicker debris accumulation, revealed strong signals of Fe and O, along with minor Ti and Al. This composition is indicative of counterface material transfer from the C45 steel disk and the formation of oxidized third-body debris, likely composed of iron oxides and tribofilms. The presence of oxygen-rich transfer layers at this early stage suggests that localized thermo chemical reactions, even under moderate mechanical loads. In contrast, the second EDX spectrum, obtained from a region containing fine abrasive dust or light transfer material, displayed dominant peaks of Ti and Al, with minimal Fe and O. The reduced iron content also indicates the adhesive and oxidative effects were present but not extensive, reflecting a localized interaction rather than widespread material transfer. These observations suggest that Pin 2 underwent mild abrasive wear, enhanced by thermal fatigue and the early onset of thermo-oxidation, without catastrophic coating failure.

The SEM and EDX findings in Figs. 10 and 11 provide microstructural and chemical evidence for the wear progression proposed in earlier sections. The observed sequence ranging from intact TiN layers to AlTiN exposure to substrate failure and third-body coverage confirms a coating degradation influenced by load, sliding speed, and duration involving various wear mechanisms.

These additional wear behaviour tests (Pins 1–5) were not part of the friction coefficient dataset but were specifically designed to cover representative regimes in the load–velocity domain relevant to the grey-box model. The observed coating failure mechanisms including TiN removal, AlTiN exposure, tribo-oxide formation, and WC substrate wear show strong correlation with the frictional and thermal regimes represented in the model. Consequently, these experiments provide a physical interpretation and validation of the input–output behaviour of the grey-box friction model presented in section 5. The findings from wear morphology (Figs. 7 and 8), elemental analysis (Figs. 10 and 11), and wear coefficients (Fig. 9) directly support the pressure- and velocity-dependent friction trends captured in the inversely optimized adhesive friction map (Fig. 17).

5. Inverse optimization of measured *COF*

After generating the dataset with the presented tribometer, a subsequent FEA modelling step is introduced to account for the following issues. The Coulomb friction coefficient can be calculated as the division of experimentally determined tangential forces F_t by the normal force F_N. However, at high normal loads applied to the pin, this calculation becomes unreliable due to the onset of plastic deformation at the tip of the pin. This deformation alters the real contact area and load distribution, introducing an additional tangential force $F_{t,def}$ that contributes to the overall *COF*. As a result, pin-on-disk tribometers tend to provide higher *COF* values compared to the adhesive *COF*. Therefore the original coulomb friction calculation results in the so called apparent friction coefficient stated in equation (6), which is based on Bowden and Tabor [28].

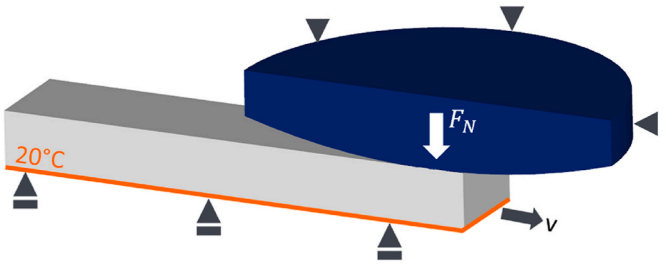

Fig. 12. Schematic of the 3D modelling approach (cross section).

Table 3
Track-width dependency on load and sliding velocity.

	Load	Sliding velocity	Track width
Run 1	150 N	75 m/min	821 µm
Run 2	150 N	150 m/min	856 µm
Run 3	750 N	75 m/min	1455 µm
Run 4	750 N	150 m/min	1437 µm
Run 5	1500 N	75 m/min	1890 µm
Run 6	1500 N	150 m/min	1896 µm

$$\mu_{app} = \frac{F_t}{F_N} = \frac{F_{t,adh}}{F_N} + \frac{F_{t,def}}{F_N} \tag{6}$$

As the *COF* is commonly described as being dependent on contact pressure, enabling the comparison of tribometers utilizing different pin geometries, such as varying diameters and radii, becomes challenging. The static Hertzian pressure σ_H stated in equation (7) was introduced to allow for a comparison of different setups. Here, σ_H is a function of the Young's moduli of the workpiece and pin material E_1 and E_2, their corresponding Poisson's ratio ν_1 and ν_2 and the normal force F_N along with the geometric dependency on the tip radius r.

$$\sigma_H = \frac{1}{\pi}\sqrt[3]{\frac{3F_N}{2r^2}\left(\frac{2E_1E_2}{(E_1+E_2)(1-\nu^2)}\right)^2} \tag{7}$$

As the dominant mechanism of sliding friction is reported to be adhesion [2], the determination of the adhesive friction coefficient can be achieved inversely by FEA while neglecting the influence of the remaining mechanisms responsible for friction namely being ploughing or plastic deformation. FEA can be utilized to calculate the adhesive friction coefficient by setting a constant *COF* of a coulomb friction model and analysing the resulting tangential forces [10]. When setting up the simulation, this work exploits the statement of Wenyi et al. [29] who stated that a the pin can be considered as sliding along a straight wear track. Plane strain is assumed. A cross-section of the model with the boundary conditions is shown in Fig. 12.

The validation of the modelling approach is vital to draw meaningful information from its results. The wear-track-width is used as the metric. With the known radius of the pin, a realistic penetration depth and most importantly a realistic deformation in front of the pin's track can be assumed. As this study aims to capture the influence of normal pressure and sliding velocity on the *COF*, the influence of both parameters on the wear track width was studied by setting up a full factorial experimental plan with three different normal loads and two different sliding velocities. An emphasis was put on the influence of the normal load as this can be expected to be the dominant influence on the widths of the wear track. Experiments were conducted for one revolution of the disk. Wear track widths were evaluated using the ALICONA G5 focus-variation microscope with 5 times magnification. The results of the experiments are listed in Table 3. Fig. 13 depicts different wear track widths according to the three loads from Table 3.

With these results from Table 3 it can be concluded that the sliding velocity which could potentially cause strain-rate hardening effects in

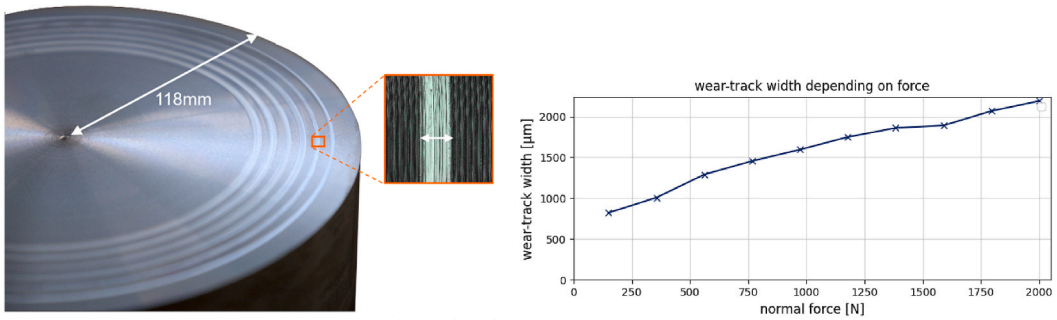

Fig. 13. Resulting wear track widths on disk after one revolution.

the disk and thus different wear track depths and widths, can be neglected as an effect for the track width. In the further study, only the influence of the normal load on the track width was studied to validate the FE model and additional force dependent track widths were measurement and depicted in Fig. 13 b. With the found wear track width and the radius at the pin of the disk, the following initial depth d of the pin can be set as a boundary condition depending on the radius of the pin r and wear track width w, as described in equation (8).

$$d = r - \sqrt{r^2 - \left(\frac{w}{2}\right)^2} \tag{8}$$

After establishing a method to set up realistic models, the simulations boundary conditions are to be determined. A normal load was applied to the pin and the workpiece was modelled as plastic and constrained in z-direction. Mesh windows were utilized to enable a locally finer mesh in the region of interest being the contact area of the pin and the disc. Automatic remeshing was employed after 10 simulation steps. The workpiece dimensions are 1 mm in height and 10 mm in length. The pin is considered a rigid body in the model.

The introduction of constitutive equations, which are a mathematical representation of the flow behaviour of materials [30] are a vital part to achieve meaningful deformation simulations. For machining operations, the Johnson-Cook (J-C) model [31] is mostly applied and relates flow stress with strain, strain-rate and temperature [32]. In equation (9) the J-C model is explained where σ is the flow stress, ε_p is the effective plastic strain, $\dot{\varepsilon_p}$ is the plastic strain rate, $\dot{\varepsilon_0}$ is the reference strain rate while T, T_m and T_0 are the test temperature, the melting point of the material and the reference temperature respectively [33]. This leaves A, B, C, n and m as the material dependent parameters [32] where A is the initial yield stress at reference strain rate and temperature, B is the hardening modulus, C is the strain rate dependency coefficient, n is the work hardening exponent and m is the thermal softening component [34].

$$\sigma = \left(A + B\varepsilon_p^n\right)\left[1 + C\,ln\left(\frac{\dot{\varepsilon_p}}{\dot{\varepsilon_0}}\right)\right]\left[1 - \left(\frac{T - T_0}{T_m - T_0}\right)^m\right] \tag{9}$$

This flow-stress model contains three parts which are the strain hardening, strain rate and thermal softening [35]. To obtain meaningful material parameters, the workpiece material should be tested under conditions that replicate those encountered during the actual machining process.

For the determination of A, B, n and m quasi static compression experiments were conducted at room temperature. To achieve this, compression experiments are carried out with a Gleeble 3800c at temperatures of 25 °C–1000 °C with an interval of 167 °C. The Gleeble 3800c is a high-performance thermo-mechanical physical simulation system designed to study metal behaviour under industrial processing conditions and features rapid resistive heating and hydraulic actuators for specimen compression. The temperature range was chosen to keep the reference temperature at room temperature while the upper

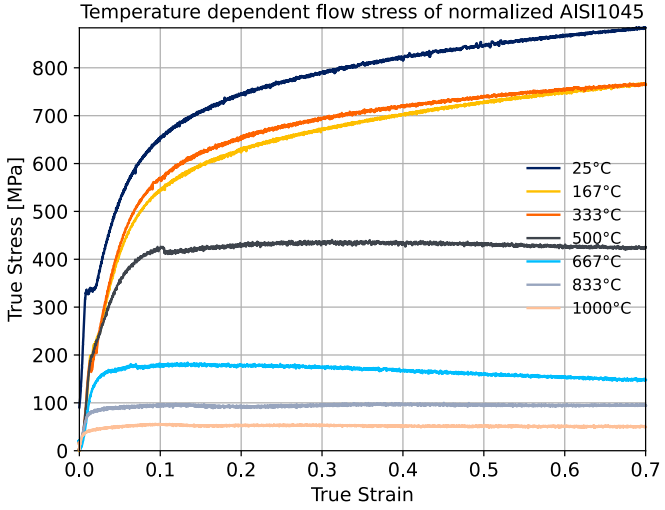

Fig. 14. Stress-strain curves measured with Gleeble 3800c.

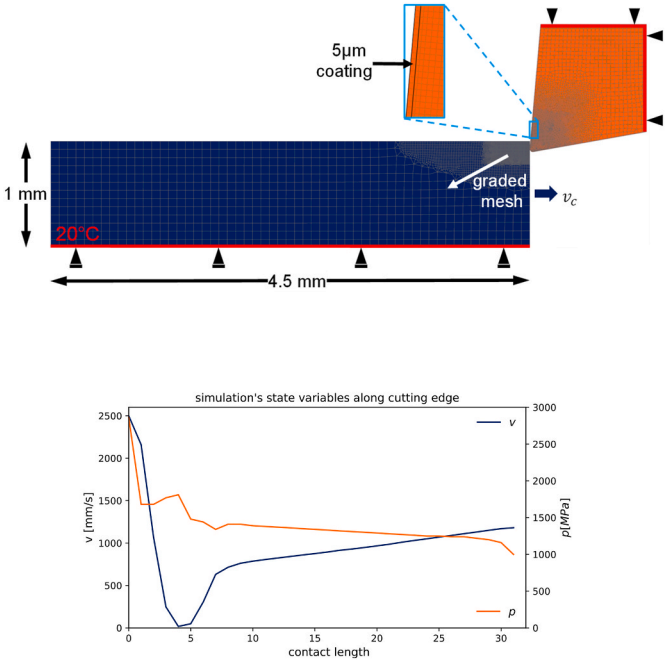

Fig. 15. Setup of the 2D cutting simulation (top) and nodes state variables along contact length (bottom).

Table 4
FEA model input parameters for AISI 1045.

Parameter	Value	Ref.
Young's modulus [GPa]	E(T)	[41]
Density [kg m^{-3}]	7850	[42]
Poisson's ratio [ ]	0.3	[43]
Thermal conductivity [W m^{-1} K^{-1}]	λ(T)	[41]
Specific heat capacity [J kg^{-1} K^{-1}]	c_p(T)	[41]
Melting temperature [K]	1773	[42]
A [MPa]	331	
B [MPa]	614	
n [ ]	0.26	
m [ ]	1.19	
C [ ]	0.045	

Table 5
FEA model input parameters for carbide.

Parameter	Value	Ref.
Thermal conductivity [$Wm^{-1}K^{-1}$]	λ(T)	[44]
Specific heat capacity [J $kg^{-1}K^{-1}$]	c_p(T)	[44]

Table 6
FEA model input parameters for AlTiN coating.

Parameter	Value	Ref.
Thermal conductivity [$Wm^{-1}K^{-1}$]	4.64 + 0.00054T	[45]
Specific heat capacity [J $kg^{-1}K^{-1}$]	c_p(T)	[46]
Coating thickness [μm]	3	

boundary resembles the expected maximum chip temperature in cutting. Thus, the material behaviour can be determined for the entire temperature range in cutting. The strain rate is kept at a minimum of $4x10^{-3}$ s^{-1}. Test specimens are in a cylindrical shape with the length of 15 mm and diameter of 10 mm. A common tolerance for specimens is a maximum deviation of 0.02 mm. The front face's centre roughness value R_a is 0.4 μm while the lateral surface area's R_a is 0.8 μm. The experimental procedure is as follows: First the specimens were heated to target temperature with an increase in temperature of 10 °C s^{-1}. After the target temperature is reached, the heating phase is followed by a delay of 120 s which ensures a uniform temperature in the specimen [36].

Thereafter, the compression tests were performed during which the load and positional displacement are recorded. The stress strain curves resulting from compression tests are shown in Fig. 14.

As expected, higher temperatures led to a significantly reduced flow stress. Notably the curve representing a compression temperature of 333 °C features higher values than the curve at 167 °C. This effect can be explained as the blue brittle region.

The mathematical procedure for determining of the material parameters is described in detail in several studies [33,37].

As the parameter ***C*** can not be fitted with these experiments, the authors decided to fit that parameter inversely via FEA while being aware that this identification has its weaknesses as it requires the definition of a friction model which yet has to be determined. A hybrid friction model with μ = 0.35 and m = 1 is chosen [38]. Cutting experiments were performed with v_c 150 m/min and a_p being 0.1 mm to determine the cutting force for model validation. The parameter ***C*** was found by utilizing the FEA software package DEFORM-2D (v. 13.1). A 2D simulation can accurately represent the cutting process when a set of boundary conditions are fulfilled, which are taken from Sadeghifar et al. [39]: The tool nose does not participate in the cutting process, the cutting tool width is larger than the width of the workpiece, the uncut chip thickness should be at least five times smaller than the width of cut, and the cutting direction must be perpendicular to the cutting edge. In most cases, a 2D orthogonal cutting simulation assumes a plane strain condition at the tool center and a plane stress condition at the tool edges

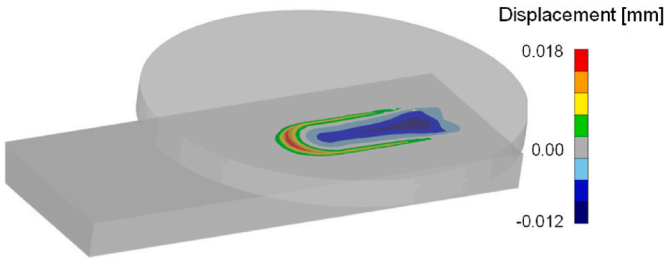

Fig. 16. Workpiece displacement in z-direction.

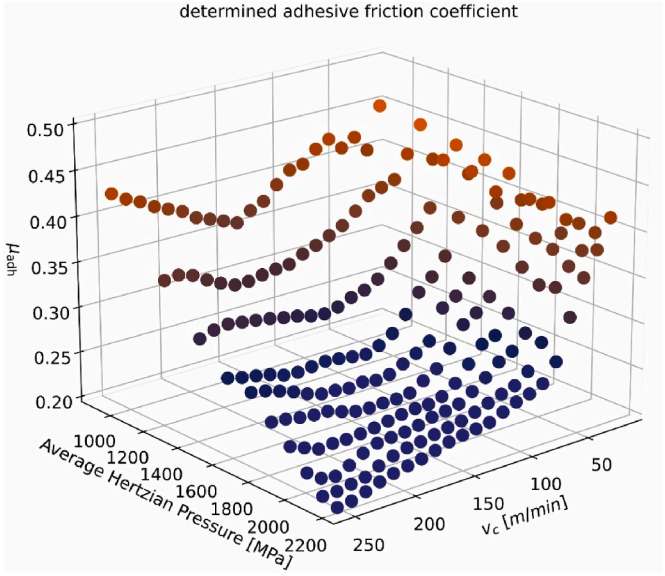

Fig. 17. Adhesive friction coefficient after inverse optimization with FEA.

[40]. Each cutting simulation was performed until the cutting force steady-state was reached. Mesh windows were utilized to improve the efficiency and the accuracy of the simulation. The mesh size of the workpiece was set to 6 μm. All material specific model input parameters for AISI 1045, the carbide and the coating are shown in Table 4, Tables 5 and 6 respectively. As the tool was modelled as rigid, no data other than thermal parameters are stated.

As a result, the J-C parameter *C* for AISI 1045 was determined as 0.045. With the determined J-C parameters, cutting simulations were performed to study the velocity and normal pressure along the tool. The boundary simulation for a simulation with a cutting depth of 0.1 mm and cutting velocity v_c of 150 m/min is shown in Fig. 15 (top). When plotting the cutting velocity and normal contact pressure along the cutting length, the following plot is derived in Fig. 15 (bottom).

With the simulation results, the presented validity of the undertaken tribometer experiments is underlined, where the average static hertzian pressure is given as 914.7 MPa and 2170 MPa for applied normal loads of 150 N and 2000 N respectively, with the assumptions from Tables 4 and 6.

Due to the pre-determined material model, this study can therefore eliminate concerns with discrepancies between the simulated and in the tribo-experiments utilized material and therefore underlines the significance of this methodology in finding accurate *COF* under machining conditions.

After specifying boundary conditions, insights in the simulation behaviour are given. For the example of applying 2000 N normal load on the pin and a set coulomb friction model of 0.25 the following information can be drawn from the simulation. The displacement of

workpiece material in z-direction is depicted in Fig. 16. This plot is validating the issue commonly found in pin on disc tribometers, as the material build up in front of the pin could be replicated by the simulation and thus the application of equation (6) is valid for the proposed simulation. Besides the buildup in sliding direction, a permanent workpiece deformation in z-direction is also noticeable to the left and right of the contact zone. Thus, the simulation features the most important criteria and can be classified as trustworthy for following investigations.

Due to the amount of generated data points, modelling all experiments in 3D is computationally expensive. When considering the inverse identification of μ_{adh}, this comes down to multiple hundred simulations. To overcome this hurdle, an equidistant simulation plan is implemented consisting of six simulations every second normal load starting from 1777 N. On average, the *COF* was reduced by 7.29 % over the measured values. Results were extrapolated for lower forces, as the simulation did not report steady force results due to contact flickering, an phenomenon described by Binder et al. [47]. After applying the found relationship to the experimentally determined values in Fig. 6 for all the determined data points, the inversely determined pressure and velocity dependent μ_{adh} is plotted in Fig. 17.

5.1. Grey-box model for cutting simulation

After determination of Fig. 17, it becomes clear that modelling this curve, which can still be considered a simplification of the *COF* as it does not consider additional parameters like influence of temperature, is an ideal use case for machine learning algorithms. Therefore, in contrast to previous friction modelling techniques, a different approach is chosen in this study to form a Grey-Box model.

As stated in Ref. [48], grey-box models are a composition of theory-driven (white-box) models f_T and data-driven (black-box) models f_D. Grey-box models can be classified as serial models, where the output of f_T is the input of f_D or vice versa or as parallel models [49]. In order to fulfil the task of accurate friction modelling, a parallel approach is chosen. In this architecture a steady stream of information is enabled between the black-box and the white-box making up the grey-box model.

Besides choosing a suitable grey-box architecture, the artificial intelligence based model f_D for the regression has to be selected. As the amount of datapoints is still comparably small when considering modern AI applications, the focus is put towards models which are known to work well with small datasets. In total, four models for f_T are studied which are random forest regression (RF), support vector regression (SVR), extreme gradient boosting (XGBoost) and Feed Forward Neural Networks (FFNN), some of which have been utilized in previous studies by the authors on small datasets within the domain of cutting force prediction [50]. Besides the selected algorithms' good performance on similar tasks, they also cover different modelling approaches within supervised learning being margin-based methods (SVR), deep function approximators (FFNN), bagging-based ensembles (RF), boosting-based ensembles (XGBoost). Thus, they provide a representative sample of widely accepted, high-performing techniques.

Random forest is a supervised machine learning technique introduced by Breiman [51], which is used for regression and classification tasks. Random forests are a scheme for building a predictor by a set of decision trees [52]. Samples are drawn based on the bagging algorithm [51]. Each tree in the ensemble is trained on a randomly sampled subset of the data, which makes the model less prone to overfitting [53]. Random forest is considered a black-box model due to the difficulty of in interpreting its internal decision logic [54]. The hyperparameter n_estimators was determined as 100 within testing 10, 50, 100 and 200 as possible options.

For all hyperparameter optimizations, the mean squared error is identified and the best performing model is selected for the final evaluation,.

Support vector regression is known for its robustness to outliers and its ability to model complex non-linear relationships. Given the generated dataset $D = \{(x_i y_i)\}_{i=1}^{n} \in R^2$ xR, the algorithm transforms input features into a high-dimensional space by the nonlinear function Φ. In this space, a linear function f is defined according to equation (10) [55], where $\varphi(x)$ is a point in the feature space. Then w and b are determined by optimizing equation (11). SVR ensures that a function $f(x)$ with ε precision exists for the entire training dataset, where ε being equal to zero represents optimum regression [56]. Slack variables ξ_i, ξ_i^* are introduced to cope with infeasible constraints of the optimization problem while $C > 0$ defines the balance between the smoothness of f and the extent to which deviations beyond ε are accepted [57]. To optimize the performance of the Support Vector Regression model, a grid search was conducted. The hyperparameter search space included values of C equal to 0.1, 1, 10, and 100, kernel types linear, polynomial, radial basis function, and sigmoid, as well as ε values of 0.01, 0.1, 0.2, and 0.5. The best-performing configuration identified through this process used a radial basis function kernel, with C set to 100 and ε set to 0.01.

$$f(x) = w^T \varphi(x) + b, w \in R^2 \wedge b \in R \tag{10}$$

$$min\ \frac{1}{2}\|w\|^2 + C\sum_{i=1}^{n}\left(\xi_i + \xi_i^*\right)$$

$$\text{subject to } \begin{cases} y_i\text{-}w^T\varphi(x)\text{-}b \le \varepsilon + \xi_i \\ w^T\varphi(x) + b\text{-}y_i \le \varepsilon + \xi_i^* \\ \xi_i, \xi_i^* \ge 0 \end{cases} \tag{11}$$

XGBoost, short for Extreme Gradient Boosting, is a tree-based supervised learning algorithm that has gained popularity due to its high scalability and run time – up to ten times quicker than earlier methods [58]. Following the formulation outlined in Ref. [59], an objective function is defined as the sum of a loss function L and a regularization component $\Omega(f_k)$ as shown in equation (12), where K is the total number of trees. The regularization term, which includes the number of leaves T and the weight of each leaf w is specified in equation (13). To ensure optimal performance, a grid search was employed to tune the hyperparameters n_estimators (100, 300, 500), max_depth (3, 5, 7), and learning_rate (0.01, 0.05, 0.1). The configuration of 500, 5 and 0.1 yielded the best results.

$$obj = \sum_{i=1}^{n} L(y_i, \widehat{y}_i) + \sum_{k=1}^{K} \Omega(f_k) \tag{12}$$

$$\Omega(f_k) = \gamma T + \frac{1}{2}\lambda\sum_{j=1}^{T} w_j^2 \tag{13}$$

Finally, a FFNN is implemented and consists of interconnected layers with an unidirectional information flow. The basis of FFNN are perceptrons, which are connected to each other [50]. In training weights w_i with $i \in [1, n]$ are updated via backpropagation [60]. Activation functions such as Rectified Linear Units (ReLU) introduce non-linear behaviour. The output y of a single neuron is calculated according to equation (14), where x_i is the input and b is the bias.

$$y = ReLU\left(\sum_{i=1}^{n} w_i x_i + b\right) \tag{14}$$

$$\text{with } ReLU(x) = \begin{cases} x, x \ge 0 \\ 0, x < 0 \end{cases} \tag{15}$$

The chosen network structure consists of two neurons in the input layer. One is used for the sliding velocity and one for the normal pressure. Two hidden layers and an output layer with one neuron are trained. A Grid-search with two hidden layers with (64, 32), (32, 16)

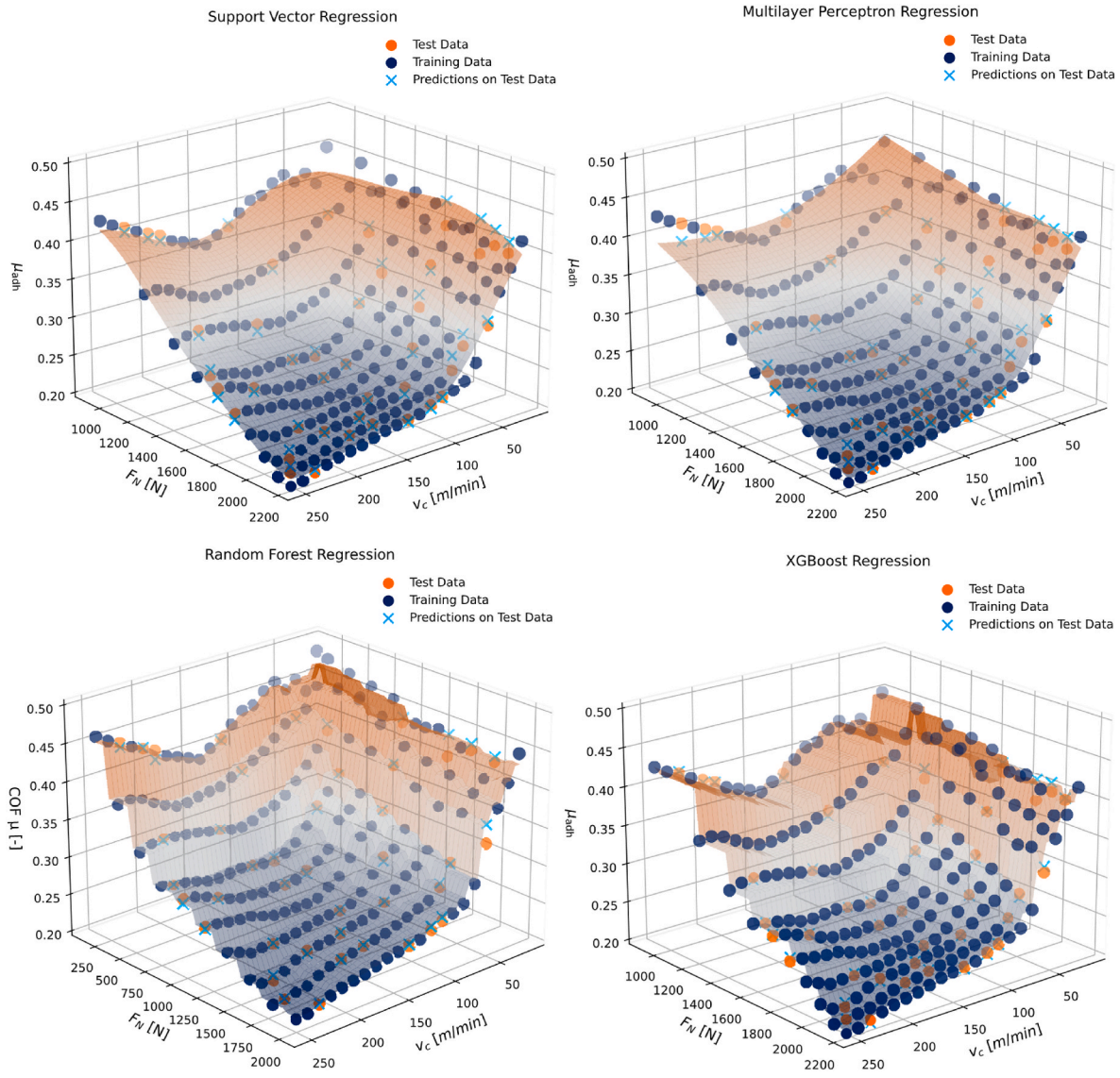

Fig. 18. Regression result of chosen algorithms.

neurons, activation functions ReLU and tanh as well as learning_rate (0.001, 0.01, 0.1) suggested to further study the configuration of (32, 16) with ReLU as activation function and 0.01 as learning rate. Considering the size of the dataset and to reduce the amount of trainable parameters, only two hidden layers were chosen.

The results of training the algorithms are depicted in Fig. 18. To extract meaningful information regarding the regression capabilities of the different algorithms the metrics mean absolute error (MAE), mean squared error (MSE) and mean absolute percentage error (MAPE) are calculated. 1000 bootstrap resamples are introduced to provide insights in the variability of model performance caused by random sampling. R^2 is given as point estimate. The results are listed in Table 7.

The training performance of all four regression models was evaluated using several error metrics. Among them, XGBoost demonstrated the best overall performance, achieving the lowest mean absolute error (MAE = 0.0025), mean squared error (MSE ≈ 0.0000) and mean absolute percentage error (MAPE = 0.0078), along with the highest coefficient of determination (R^2 = 0.9913). Random Forest followed closely, also showing strong predictive accuracy with MAE = 0.0048 and R^2 = 0.9890. The Support Vector model showed slightly higher errors (MAE = 0.0090, R^2 = 0.9670), while the FFNN model performed well (MAE = 0.0052, R^2 = 0.9737). The confidence intervals for MAPE and MAE were narrowest for XGBoost and Random Forest, indicating greater stability and robustness of these models. In contrast, FFNN showed a markedly wider upper bound in its MAPE interval (up to 0.316), suggesting variability in relative prediction accuracy. Overall, tree-based ensemble methods (RF and XGBoost) outperformed SV and FFNN in the training phase, both in terms of point estimates and confidence intervals, highlighting their superior capability in capturing the underlying patterns of the data with consistent reliability.

Table 7
Evaluation metrics for implemented regression models with 95 % confidence intervals (CI).

		SV	RF	XGBoost	FFNN
MAE	μ	0.009	0.0048	0.0025	0.0052
	CI_-	0.0064	0.0033	0.0027	0.0059
	CI_+	0.0118	0.0066	0.0058	0.0110
MSE	μ	0.0001	0.0000	0.0000	0.0001
	CI_-	0.0001	0.0000	0.0000	0.0001
	CI_+	0.0003	0.0001	0.0001	0.0002
R^2		0.9670	0.9890	0.9913	0.9737
MAPE	μ	0.0192	0.0094	0.0078	0.0178
	CI_-	0.0202	0.0103	0.0088	0.0179
	CI_+	0.0346	0.0191	0.0164	0.316

Table 8
Mean feature importance calculation via permutation.

	SV	RF	XGBoost	FFNN
v_c	1.0377	0.9824	0.9952	1.0141
F_N	0.9056	0.9271	0.9486	0.9164

By utilizing sklearn.inspection with 30 repeats for each feature and a random state of 42, the relative influence of the input features v_c and F_N on model predictions was determined for each model via permutation and listed in Table 8.

As shown in Table 8, all models consistently attribute slightly higher importance to v_c compared to F_N. XGBoost and the neural network models showed the most balanced use of both features, with v_c importances of 0.9952 and 1.0141, and F_N importance of 0.9486 and 0.9164 respectively. Random Forest also demonstrated a similar pattern, with importance values of 0.9824 for v_c and 0.9271 for F_N. The Support Vector model showed the largest relative gap between the two features. These results indicate that while both features are relevant across all models, cutting speed v_c tends to have a slightly stronger effect on the predicted coefficient of friction. The consistency of this trend across diverse model architectures underlines the conclusion that v_c is marginally more influential in the modelled physical relationship.

6. Implementation of a python interface for DEFORM 2D

In general most FEA softwares provide the user with user subroutines enabling them to make custom changes to the FEA engine e.g. for the definition of a custom temperature dependent friction model. However, these subroutines are written in Fortran which does not allow for the easy implementation of most AI libraries. This lead to researchers abandoning more elevated friction models due to the lack of options to integrate them into FEA and more traditional models were instead employed, as also reported by Puls et al. [15]. To overcome this hurdle in introducing data driven friction models to cutting simulations, a custom Python-interface was implemented, parts of which were introduced by Wolf et al. [61]. Our approach eliminates the need to manually implement AI tools in Fortran code, instead leveraging a Python interface that directly incorporates widely used AI libraries available in Python. This low-barrier integration significantly simplifies the adoption of advanced AI techniques within FEA simulations. The concept is based on the conversion of databases, which essentially are files interpretable by the DEFORM FEA engine, into text-files, which contain the information of the simulation e.g. coordinates, stress and temperature of each node. These text-files can be interpreted by humans which allows the alteration of model input parameters such as the applied friction law. Since DEFORM provides the possibility to start a simulation with a command line input that passes the name of the database of interest to the FEA solver, and furthermore specifies the number of the future steps to be calculated, it is possible to fully automate the execution of a simulation as following: An initial database is generated in DEFORM, the Python algorithms starts the simulation for the specified number of steps, converts the new database to a text file, reads the textfile, alters model input parameters and the number of executable steps of the new simulation, converts it back to a database and finally executes the new database by another command line input. This approach is graphically illustrated in Fig. 19.

A benefit of DEFORM is the introduction of friction windows, inside which a local friction law can be specified. Thus, any contact between the tool and chip or the tool and workpiece inside this friction window will be treated in accordance to the locally defined friction model. By

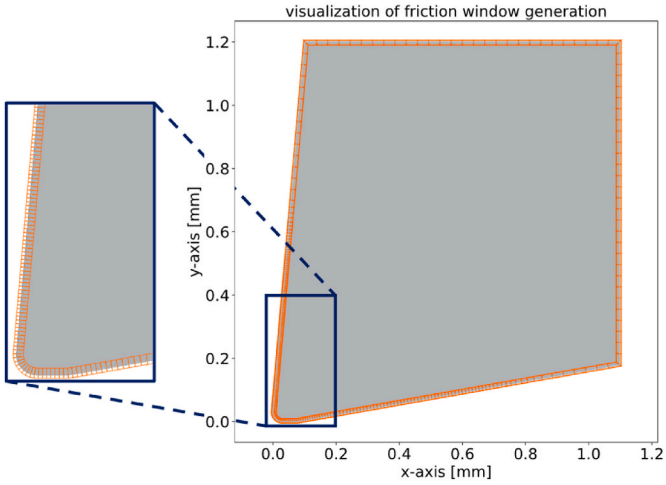

Fig. 20. Result of friction window definition algorithm.

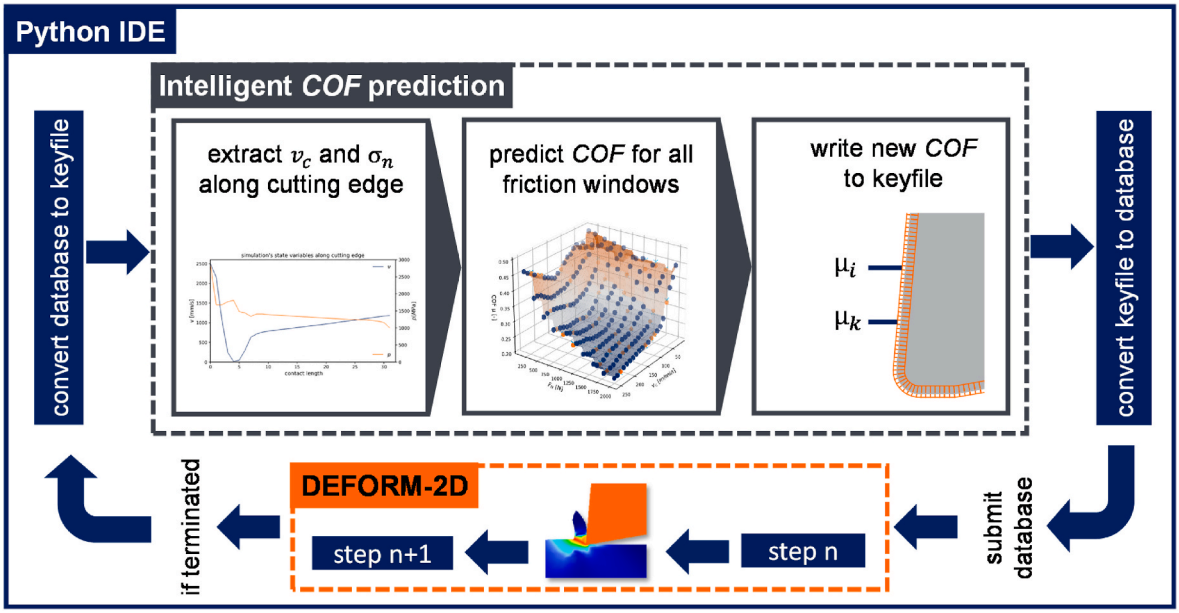

Fig. 19. Python interface enabling data driven input of friction model.

extracting the local normal pressures and sliding velocities along the tool-chip interface, and matching the position of the nodes in contact to the friction windows coordinates, the *COF* can be predicted by an AI model utilizing prominent Python libraries. Thus, this approach allows for the integration AI into FEA and forms a Grey-Box cutting simulation framework while at the same time omitting the usage of Fortran user subroutines. The definition of the friction windows shown in Fig. 20 was performed as follows.

First, a database without friction windows was defined, where the mesh at the surface of the tool is sized according to the aimed size of the friction windows. Then the database is converted to a keyfile with the previously described methods. As the thickness of the coating is selected to be one element, all elements containing to the material group of the coating automatically make up the outer mesh. Once these elements are stored in a list, the corresponding nodes to each element are collected. Then the vector pointing from in to outside is determined by the coordinates of the nodes and the 4 points in space making up the mesh window are defined. The last step consists of printing the friction windows with the definition of an initial friction law for the first step to the keyfile. After then converting this file to the starting database, a simulation can be run with the automatically defined friction windows.

7. Conclusion

Understanding the frictional behaviour of tool coatings is crucial for characterising tribo-mechanical interactions in metal cutting and for the development of advanced wear-resistant coatings. This study contributes to this goal by introducing a novel tribometer capable of replicating the high sliding velocities and contact pressures typically observed in cutting operations. Through systematic tribological testing and advanced surface analysis, several important findings emerged.

- Under machining conditions, the *COF* is not only dependent on sliding velocity, as previously emphasized in literature, but also shows a significant dependency on contact pressure. This highlights the need to consider pressure effects explicitly in friction modelling.
- The wear performance of TiN/AlTiN-coated WC pins under dry sliding conditions was found to depend on the combined effects of sliding speed and duration rather than on applied load alone. High-speed tests led to thermal-mechanical overload and coating delamination, whereas low-speed, long-duration tests resulted in fatigue-driven wear without full coating failure. Moderate conditions preserved coating integrity, emphasizing the protective role of the multilayer structure, particularly the resilience of the AlTiN layer when the TiN top layer begins to fail.
- The study introduced a novel Python-based framework to locally predict the COF using trained artificial intelligence models. Several machine learning approaches (support vector regression, random forest, feedforward neural network and XGBoost) were evaluated, with XGBoost demonstrating the highest prediction accuracy. Feature importance analysis confirmed that both normal force and cutting speed are essential inputs for reliable *COF* prediction.
- This AI-driven predictive model was successfully integrated into the DEFORM finite element analysis software through a custom Python interface. This Grey-Box approach overcomes traditional limitations in incorporating complex, data-driven friction models into FEA environments.

CRediT authorship contribution statement

Jan Wolf: Writing – review & editing, Writing – original draft, Visualization, Validation, Software, Methodology, Investigation, Formal analysis, Data curation, Conceptualization. **Nithin Kumar Bandaru:** Writing – review & editing, Writing – original draft, Visualization, Validation, Investigation, Formal analysis. **Martin Dienwiebel:** Writing – review & editing, Supervision, Resources, Project administration, Funding acquisition. **Hans-Christian Möhring:** Writing – review & editing, Supervision, Resources, Project administration, Funding acquisition.

Declaration of competing interest

The authors declare that they have no known competing financial interests or personal relationships that could have appeared to influence the work reported in this paper.

Acknowledgements

The scientific work has been supported by the German Research Foundation (DFG) within the research priority program SPP 2402 with project number 521378544. The authors thank Paul Horn GmbH for generously providing the coated pins and tools.

Data availability

Data will be made available on request.

References

[1] D. Mourtzis, M. Doukas, D. Bernidaki, Simulation in manufacturing: review and challenges, Proced. CIRP 25 (2014) 213–229, https://doi.org/10.1016/j.procir.2014.10.032.
[2] S.N. Melkote, W. Grzesik, J. Outeiro, J. Rech, V. Schulze, H. Attia, P.-J. Arrazola, R. M'Saoubi, C. Saldana, Advances in material and friction data for modelling of metal machining, CIRP Annals 66 (2017) 731–754, https://doi.org/10.1016/j.cirp.2017.05.002.
[3] M. Abouridouane, T. Bergs, D. Schraknepper, G. Wirtz, Friction behavior in metal cutting: modeling and simulation, Proced. CIRP 102 (2021) 405–4010, https://doi.org/10.1016/j.procir.2021.09.069.
[4] M.E. Merchant, Mechanics of the metal cutting process. II. Plasticity conditions in orthogonal cutting, J. Appl. Phys. 16 (1945) 318–324, https://doi.org/10.1063/1.1707596.
[5] E. Ceretti, L. Filice, D. Umbrello, F. Micari, ALE simulation of orthogonal cutting: a new approach to model heat transfer phenomena at the tool-chip interface, CIRP Annals 56 (2007) 69–72, https://doi.org/10.1016/j.cirp.2007.05.019.
[6] M. Du, Z. Cheng, S. Wang, Finite element modeling of friction at the tool-chip-workpiece interface in high speed machining of Ti6Al4V, Int. J. Mech. Sci. 163 (2019) 105100, https://doi.org/10.1016/j.ijmecsci.2019.105100.
[7] M. Binder, F. Klocke, D. Lung, Tool wear simulation of complex shaped coated cutting tools, Wear (2015) 600–607, https://doi.org/10.1016/j.wear.2015.01.015.
[8] F. Zanger, P. Bollig, V. Schulze, Simulative investigations on different friction coefficient models, Proced. CIRP 58 (2017) 140–145, https://doi.org/10.1016/j.procir.2017.03.203.
[9] M. Olsson, S. Söderberg, S. Jacobsen, S. Hogmark, Simulation of cutting tool wear by a modified PIN-ON-disc test, Int. J. Mach. Tools Manufact. 29 (1989) 377–390.
[10] H. Ben Abdelali, C. Courbon, J. Rech, W. Ben Salem, A. Dogui, P. Kapsa, Identification of a friction model at the tool-chip-workpiece interface in dry machining of a AISI 1045 steel with a TiN coated carbide tool, J. Tribol. 133 (2011) 042201.
[11] D. Smolenicki, J. Boos, F. Kuster, H. Roelofs, C.F. Wyen, In-process measurement of friction coefficient in orthogonal cutting, CIRP Ann. - Manuf. Technol. 63 (2014) 97–100, https://doi.org/10.1016/j.cirp.2014.03.083.
[12] V. Schulze, F. Bleicher, C. Courbon, M. Gerstenmeyer, L. Meier, J. Philipp, J. Rech, J. Schneider, E. Segebade, A. Steininger, K. Wegener, Determination of constitutive friction laws appropriate for simulation of cutting processes, CIRP J. Manuf. Sci. Technol. 38 (2022) 139–158, https://doi.org/10.1016/j.cirpj.2022.04.008.
[13] J. Rech, C. Claudin, P. Polly, C. Courbon, New aspects of metrology of frictional behaviour in metal cutting, Mechanik (2016) 1751–1753, https://doi.org/10.17814/mechanik.2016.11.520.
[14] T. Leveille, D. Fabre, M. Cici, J. Sijobert, M. Doubenskaia, C. Courbon, Development of a novel high temperature open tribometer with laser-based heating system, Wear 477 (2021) 203881, https://doi.org/10.1016/j.wear.2021.203881.
[15] H. Puls, F. Klocke, D. Lung, Experimental investigation on friction under metal cutting conditions, Wear 310 (2014) 63–71, https://doi.org/10.1016/j.wear.2013.12.020.
[16] P.J. Arrazola, T. Özel, Investigations on the effects of friction modeling in finite element simulation of machining, Int. J. Mech. Sci. 52 (2010) 31–42, https://doi.org/10.1016/j.ijmecsci.2009.10.001.
[17] P. Volke, C. Courbon, E. Krumme, J. Saelzer, D. Biermann, Frictional behaviour of coated carbide tools and AISI 316L when using translational and rotatory relative movement considering dry and lubricated conditions, CIRP J. Manuf. Sci. Technol. 51 (2024) 36–46, https://doi.org/10.1016/j.cirpj.2024.03.011.
[18] M. Hardt, D. Schraknepper, T. Bergs, Investigations on the application of the downhill-simplex-algorithm to the inverse determination of material model

parameters for FE-machining simulations, Simulat. Model. Pract. Theor. 107 (2021) 102214, https://doi.org/10.1016/j.simpat.2020.102214.
[19] F. Ducobu, O. Pantalé, B. Lauwers, Predictive 3D modelling of free oblique cutting introducing an ANN-based material flow law with experimental validation over a wide range of conditions, Int. J. Adv. Manuf. Technol. 131 (2024) 921–934, https://doi.org/10.1007/s00170-024-12956-7.
[20] F. Zemzemi, J. Rech, W. Ben Salem, A. Dogui, P. Kapsa, Identification of a friction model at tool/chip/workpiece interfaces in dry machining of AISI4142 treated steels, J. Mater. Process. Technol. 209 (2009) 3978–3990, https://doi.org/10.1016/j.jmatprotec.2008.09.019.
[21] I.L. Singer, S. Fayeull, P.D. Ehni, Friction and wear behavior of TiN in air: the chemistry of transfer films and debris formation, Wear (1991) 375–394.
[22] S. Wilson, A. Alpas, TiN coating wear mechanisms in dry sliding contact against high speed steel, Surf. Coating. Technol. 108–109 (1998) 369–376, https://doi.org/10.1016/S0257-8972(98)00593-3.
[23] S. Wilson, A. Alpas, Wear mechanism maps for TiN-coated high speed steel, Surf. Coating. Technol. 120–121 (1999) 519–527, https://doi.org/10.1016/S0257-8972(99)00414-4.
[24] L. Kara, D. Özkan, M. Barış Yağcı, E. Sulukan, Y. Sert, T. Sonsuz Sert, Friction and wear behaviors of TiN coatings under dry and vacuum conditions, Tribol. Trans. 62 (2019) 362–373, https://doi.org/10.1080/10402004.2018.1559385.
[25] G. Zheng, G. Zhao, X. Cheng, R. Xu, J. Zhao, H. Zhang, Frictional and wear performance of TiAlN/TiN coated tool against high-strength steel, Ceram. Int. 44 (2018) 6878–6885, https://doi.org/10.1016/j.ceramint.2018.01.113.
[26] V. Tebaldo, L. Kilpi, H. Ronkainen, M.G. Faga, Tribological properties of AlTiN coating in sliding contact with Ti6Al4V: a helpful tool for disentangling the phenomena complexity during real turning operations, Tribol. Int. 123 (2018) 71–80, https://doi.org/10.1016/j.triboint.2018.02.023.
[27] S. Król, L. Ptacek, Z. Zalisz, M. Hepner, Friction and wear properties of titanium and oxidised titanium in dry sliding against hardened C45 steel, J. Mater. Process. Technol. 157–158 (2004) 364–369, https://doi.org/10.1016/j.jmatprotec.2004.09.057.
[28] F.P. Bowden, D. Tabor, The Friction and Lubrication of Solids, Repr, Clarendon Pr, Oxford, 2008.
[29] Y. Wenyi, P. O'Dowd Noel, E.P. Busso, Numerical study of sliding wear caused by a loaded pin on a rotating disc, J. Mech. Phys. Solid. 50 (2002) 449–470, https://doi.org/10.1016/S0022-5096(01)00093-X.
[30] N. Duc-Toan, B. Tien-Long, J. Dong-Won, Y. Seung-Han, K. Young-Suk, A modified Johnson–Cook model to predict stress-strain curves of Boron steel sheets at elevated and cooling temperatures, high temp, Mater. Process. 31 (2012) 37–45, https://doi.org/10.1515/HTMP.2011.127.
[31] G.R. Johnson, W.H. Cook, A constitutive model and data for metals subjected to large strains, high strain rates, and high temperatures, in: Proceedings 7th International Symposium on Ballistics, 1983, pp. 541–547.
[32] N. Ojal, H.P. Cherukuri, T.L. Schmitz, K.T. Devlugt, A.W. Jaycox, A combined experimental and numerical approach that eliminates the non-uniqueness associated with the Johnson-Cook parameters obtained using inverse methods, Int. J. Adv. Manuf. Technol. 120 (2022) 2373–2384, https://doi.org/10.1007/s00170-021-08640-9.
[33] X. Zhang, W. Yao, X. Zhu, Z. Hu, W. Zhu, H. Huang, W. Li, Determination of Johnson–Cook constitutive of 15-5 PH steel processed by selective laser melting, Materials 800 (2023), https://doi.org/10.3390/ma16020800.
[34] N.E. Karkalos, A.P. Markopoulos, Determination of Johnson-Cook material model parameters by an optimization approach using the fireworks algorithm, Procedia Manuf. 22 (2018) 107–113, https://doi.org/10.1016/j.promfg.2018.03.017.
[35] Y. Wang, X. Zeng, H. Chen, X. Yang, F. Wang, L. Zeng, Modified Johnson-Cook constitutive model of metallic materials under a wide range of temperatures and strain rates, Results Phys. (2021) 104498, https://doi.org/10.1016/j.rinp.2021.104498.
[36] J. Priest, H. Ghadbeigi, S. Ayvar-Soberanis, A. Liljerehn, M. Way, A modified Johnson-Cook constitutive model for improved thermal softening prediction of machining simulations in C45 steel, Proced. CIRP 108 (2022) 106–111, https://doi.org/10.1016/j.procir.2022.03.022.
[37] S. Khare, K. Kumar, S. Choudhary, P.K. Singh, R.K. Verma, P. Mahajan, Determination of Johnson–Cook material parameters for armour plate using DIC and FEM, Met. Mater. Int. 27 (2021) 4984–4995, https://doi.org/10.1007/s12540-020-00895-3.
[38] C. Cappellini, A. Abeni, Development and implementation of crater and flank tool wear model for hard turning simulations, Int. J. Adv. Manuf. Technol. 120 (2022) 2055–2073, https://doi.org/10.1007/s00170-022-08885-y.
[39] M. Sadeghifar, R. Sedaghati, W. Jomaa, V. Songmene, M. Sadeghifar, R. Sedaghati, W. Jomaa, V. Songmene, A comprehensive review of finite element modeling of orthogonal machining process: chip formation and surface integrity predictions, Int. J. Adv. Manuf. Technol. 96 (2018) 3747–3791, https://doi.org/10.1007/s00170-018-1759-6.
[40] H.-C. Möhring, C. Menze, K. Drewle, D. Fackelmann, J. Stegmann, S. Kabelac, A Novel Approach for Simulating a Sawing Process with Reduced Simulation Time, CIRP JMST, 2023, pp. 72–80.
[41] M. Spittel, T. Spittel, Steel symbol/number: C45/1.0503, in: M. Spittel, T. Spittel, H. Warlimont, H. Landolt, R. Börnstein, W. Martienssen (Eds.), Numerical Data and Functional Relationships in Science and Technology: New Series, Springer, Berlin, 2009, pp. 210–215.
[42] M. Afrasiabi, J. Saelzer, S. Berger, I. Iovkov, H. Klippel, M. Röthlin, A. Zabel, D. Biermann, A numerical-experimental study on orthogonal cutting of AISI 1045 steel and Ti6Al4V alloy: SPH and FEM modeling with newly identified friction coefficients, Metals 186 (2021), https://doi.org/10.3390/met11111683.
[43] Jan Wolf, Rocco Eisseler, Nithin Kumar Bandaru, Martin Dienwiebel, Hans-Christian Möhring, A novel approach for modelling loads on profiled cutting tools, Proced. CIRP (2025) 394–399, https://doi.org/10.1016/j.procir.2025.02.068.
[44] G.E. Spriggs, 13.4 Properties of hardmetals and cermets, in: P. Beiss, R. Ruthardt, H. Warlimont, G. Leichtfried, H. Landolt, R. Börnstein, W. Martienssen, O. Madelung (Eds.), Numerical Data and Functional Relationships in Science and Technology: New Series, Springer, Berlin, 2002, pp. 86–117.
[45] J. Martan, P. Benĕs, Thermal properties of cutting tool coatings at high temperatures, Thermochim. Acta (2012) 52–55, https://doi.org/10.1016/j.tca.2012.03.029.
[46] J. Zhao, Z. Liu, B. Wang, J. Hu, PVD AlTiN coating effects on tool-chip heat partition coefficient and cutting temperature rise in orthogonal cutting Inconel 718, Int. J. Heat Mass Tran. 163 (2020) 120449, https://doi.org/10.1016/j.ijheatmasstransfer.2020.120449.
[47] M. Binder, F. Klocke, B. Doebbler, An advanced numerical approach on tool wear simulation for tool and process design in metal cutting, Simulat. Model. Pract. Theor. (2017) 65–82, https://doi.org/10.1016/j.simpat.2016.09.001.
[48] N. Takeishi, A. Kalousis, Deep grey-box modeling with adaptive data-driven models toward trustworthy estimation of theory-driven models, in: Proceedings of the 26th International Conference on Artificial Intelligence and Statistics vol 206, 2023, pp. 4089–4100.
[49] P. Menesklou, T. Sinn, H. Nirschl, M. Gleiss, Grey box modelling of decanter centrifuges by coupling a numerical process model with a neural network, Minerals 755 (2021), https://doi.org/10.3390/min11070755.
[50] T. Reeber, J. Wolf, H.-C. Möhring, A data-driven approach for cutting force prediction in FEM machining simulations using gradient boosted machines, J. Manufact. Mater. Process. 107 (2024), https://doi.org/10.3390/jmmp8030107.
[51] L. Breiman, Random Forests, vol 45, Mach Lean, 2001, pp. 5–32.
[52] G. Biau, Analysis of a random forests model, J. Mach. Learn. Res. 13 (2012) 1063–1095, https://doi.org/10.48550/arXiv.1005.0208.
[53] E. Jonssnon, S. Fredrikson, An investigation of how well random forest regression can predict demand. https://www.diva-portal.org/smash/get/diva2:1594694/FULLTEXT01.pdf, 2021. (Accessed 12 January 2025).
[54] R. Couronné, P. Probst, A.-L. Boulesteix, Random forest versus logistic regression: a large-scale benchmark experiment, BMC Bioinf. 270 (2018), https://doi.org/10.1186/s12859-018-2264-5.
[55] M. Sabzekar, S. Hasheminejad, Robust regression using support vector regressions, Chaos Solitons Fractals (2021) 110738, https://doi.org/10.1016/j.chaos.2021.110738.
[56] S.D. Agustina, O. Mustakim, C. Bella, M.A. Ramadhan, Support vector regression algorithm modeling to predict the availability of foodstuff in Indonesia to face the demographic bonus, J. Phys.: Conf. Ser. (2018) 012240, https://doi.org/10.1088/1742-6596/1028/1/012240.
[57] A.J. Smola, B. Schölkopf, A tutorial on support vector regression, Stat. Comput. 14 (2004) 199–222, https://doi.org/10.1023/B:STCO.0000035301.49549.88.
[58] T. Chen, C. Guestrin, XGBoost: a scalable tree boosting system, in: Proceedings of the 22nd ACM SIGKDD International Conference on Knowledge Discovery and Data Mining, 2016, pp. 785–794, https://doi.org/10.1145/2939672.2939785, vol 11.
[59] C. Sheng, H. Yu, An optimized prediction algorithm based on XGBoost, in: 2022 International Conference on Networking and Network Applications (NaNA), Urumqi, China, IEEE, 2022, pp. 1–6.
[60] B. Mehlig, Machine Learning with Neural Networks: an Introduction for Scientists and Engineers, Cambridge University Press, 2021.
[61] J. Wolf, T. Reeber, N.K. Bandaru, M. Dienwiebel, H.-C. Möhring, Transient wear modelling of coated cutting tools, Proced. CIRP 130 (2024) 1827–1831, https://doi.org/10.1016/j.procir.2024.10.323.